PLOS CLIMATE

RESEARCH ARTICLE

Linear response of deep ocean to a moving tropical cyclone

Ryo Furue[1]*, **Yoshio Fukao**[1], **Hiroko Sugioka**[2]

1 JAMSTEC, Yokohama, Japan, **2** Kobe University, Kobe, Japan

* ryofurue@gmail.com

Citation: Furue R, Fukao Y, Sugioka H (2024) Linear response of deep ocean to a moving tropical cyclone. PLOS Clim 3(12): e0000376. https://doi.org/10.1371/journal.pclm.0000376

Editor: Valerio Lembo, CNR: Consiglio Nazionale delle Ricerche, ITALY

Received: February 5, 2024

Accepted: August 27, 2024

Published: December 17, 2024

Peer Review History: PLOS recognizes the benefits of transparency in the peer review process; therefore, we enable the publication of all of the content of peer review and author responses alongside final, published articles. The editorial history of this article is available here: https://doi.org/10.1371/journal.pclm.0000376

Data Availability Statement: The JCOPE-T data is provided as Supporting Information except for the vertical velocity field, which is published as https://doi.org/10.5281/zenodo.13132471. The bottom-pressure observation is provided as Supporting information. The "best track" data is available from

Abstract

To explore the impacts of a moving tropical cyclone (TC) on the deep ocean, a linear continuously stratified model is solved by the method of solving for the temporal and horizontal structure of each vertical mode. The response of the barotropic mode to the TC's pressure gradient is an isostatic balance, where the sea level rise almost completely cancel the atmospheric low pressure. The response of the barotropic mode to the winds is a permanent sea level drop behind the TC. The horizontal extent of this response is determined by the distribution of the weak negative wind curl outside the core of the strong positive curl. The baroclinic response to the winds is dominated by the well-known train of near-inertial oscillation behind the TC. In addition, there is a mean upwelling and a resultant cooling. The lateral scale of the first upwelling behind the TC is determined by the size of the TC's positive curl core; further behind in the TC's wake, this feature spreads laterally at the group speed of inertio-gravity waves for the mode. The three-dimensional structure is then constructed by superposing these vertical modes. The position of the first upwelling peak coincides between the baroclinic modes; this alignment results in a vertical column of upwelling. Further down the wake, this coherence is gradually lost because of slight difference in the streamwise wavelength between modes. Also, lower vertical modes dominate further away from the TC track because of faster lower modes. A uniform-density ocean shows a similar columnar upwelling and downwelling pattern as a response to the same wind curl. The pressure anomaly field at the ocean bottom is dominated by the barotropic response to winds, modified by the baroclinic response. The near-inertial oscillation reaches the bottom quickly because of the columnar response.

1 Introduction

An array of pressure gauges installed on the sea floor at a depth of about 5000 m south of Japan [1] detected a slow pressure drop of 2–3 hPa peaking 1–2 d after the nearby passage of the center of a tropical cyclone (TC; Fig 1). The bottom pressure variability due to the weight of the water column (p_o) is dominated (not shown) by the sea-level variability ($\rho g \eta$). The atmospheric pressure anomaly (p_a) is largely canceled by p_o and the variability of the total bottom pressure ($p_o + p_a$) is much smaller than that of p_a or p_o. The observed bottom pressure appears

RMSC Tokyo (https://www.jma.go.jp/jma/jma-eng/jma-center/rsmc-hp-pub-eg/besttrack.html) of Japan Meteorological Agency.

Funding: YF and HS were partially supported by JSPS KAKENHI Grant Number JP25247074. The funder had no role in study design, data collection and analysis, decision to publish, or preparation of the manuscript.

Competing interests: The authors have declared that no competing interests exist.

to start to drop during 2015-08-10 and to reach its minimum at about the end of 2015-08-12. The corresponding time series from our OGCM (described in Section S1.1.2 in S1 Text) agrees with the observation fairly well. This agreement suggests that the observed bottom-pressure change is due to some systematic ocean circulation. Is this bottom-pressure change a direct response of the ocean to the TC, an indirect response via some oceanic processes, or a totally independent phenomenon from the TC? If it is indeed a direct response, exactly what determines its strength and its horizontal structure? More generally, how does the deep ocean respond to a moving TC?

1.1 Upwelling and deep impacts

It is well known that the Ekman divergence due to the TC's positive wind curl results in upwelling into, and cooling of, the mixed layer [e.g., 3, and references therein]. This cold wake is known to last at least for several days [e.g., 4, 5, and references therein]. A typical TC moves faster than the local baroclinic gravity waves [e.g., 6] and as a result this upwelling system leaves a trailing near-inertial oscillation, a feature that has been extensively studied observationally, theoretically, and numerically [e.g., 3, 7, and references therein].

Recently Yang *et al.* [8] reported impacts of downwelling on the mixed layer temperature in the lee of TCs and argued that the negative wind curl of the TC contributes to the warming.

Impacts of TC potentially extend to deep ocean. Kuwano-Yoshida *et al.* [9] reported a strong upwelling that reaches the bottom associated with an *explosive cyclone* in a high-resolution oceanic general circulation model (OGCM). Pedrosa-Pàmies *et al.* [10] reported that a hurricane in the mid North Atlantic enhanced vertical fluxes of organic materials at depths of 1500–3000 m. Spencer *et al.* [11] analyzed horizontal velocity anomaly associated with a Hurricane measured by moorings installed on the continental slope in the Gulf of Mexico near the bottom at ∼1500 m.

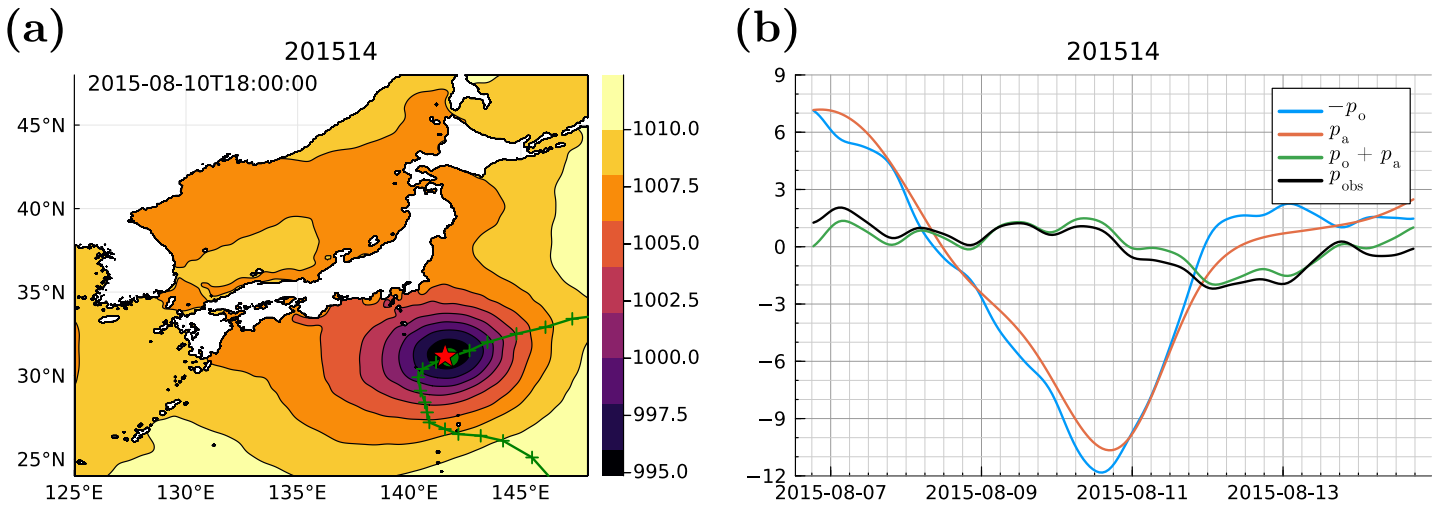

Fig 1. (A) Typhoon 1514 (No. 14 of the year 2015), which passed very near the array of bottom pressure gauges of [1] (indicated by the star). The color shading shows the sea-level atmospheric pressure at 2015-08-10T18:00:00Z, when the estimated typhoon's center is closest to the observation station, from a re-analysis product which forces our OGCM (see Section S1.1.2 in S1 Text). The observed/estimated positions (cross symbols) of the typhoon's center are from the "best track" dataset (Section S1.1.1 in S1 Text) at a 6-hr interval and the green filled circle is the position at the time of the atmospheric pressure map. (B) Time series of low-pass-filtered pressure anomalies at the observation station: sea-level atmospheric pressure (p_a, red), ocean-only pressure at the bottom from our OGCM ($p_o|_{z=-D}$, blue), observed bottom pressure anomaly (S1 Dataset) from Fukao *et al.*'s [1] dataset (black), and bottom pressure anomaly from our OGCM ($p_a + p_o|_{z=-D}$, green). To show the similarity between p_o and p_a, the sign of the former is flipped. Each anomaly is calculated by subtracting the temporal average over ±4 d about the central time of Panel A. The low-pass filter has been applied to each time series to reduce tides, which dominate the raw bottom-pressure anomalies (not shown); the filter uses the 48-hour Hann window [2].

https://doi.org/10.1371/journal.pclm.0000376.g001

What is the vertical structure of this upwelling and downwelling? What determines its location? What are the impacts of the near-inertial oscillation near the sea floor?

1.2 Linear models

Geisler [7] used a linear two-layer model, derived second-order partial differential equations that describe the equilibrium response of the vertical velocity and interfacial displacement separately for the barotropic and baroclinic modes to a pressure anomaly and wind curl of a moving TC. They showed the Green's function for each of the barotropic and barotropic responses and explained various properties of the TC response, including the train of near-inertial oscillation behind the TC. Their solutions predict that the first peak of upwelling comes a quarter wavelength of the near-inertial oscillation. They also showed that the sea level permanently drops and the thermocline is permanently raised behind the TC as an upstream integration of the barotropic and baroclinic vertical velocities, respectively.

Shay *et al.* [12] studied oceanic horizontal velocity field measured with airborne expendable current profilers (AXCPs) over the top $\sim$500 m. To understand the velocity field, they extended Geisler's [7] model to a linear continuously stratified (LCS) ocean, expressing the 3-d flow field as a superposition of 10 baroclinic vertical modes. They obtained a good agreement between the observation and the theoretical result.

1.3 Present study

The present paper is a follow-up study to [7] and the theoretical part of [12]. We construct a complete 3-d response, including both baroclinic and barotropic responses, of the LCS ocean to wind stress and atmospheric pressure of an idealized empirical-model typhoon. Particular attention is payed to the vertical and horizontal structure of the vertical velocity and pressure anomaly from the sea surface to the bottom and what determines these.

Geisler [7] looked at Green's functions to infer the properties of the ocean response. Shay *et al.* [12] used a Rankin vortex as a model TC (Section S1.4 in S1 Text) likely because of its simplicity. We extend their works by constructing responses to a more realistic wind curl and pressure. We show that the negative wind curl outside of the TC core, though weak, has significant impact on the horizontal extent of the ocean response.

The rest of the paper is organized as follows. Section 2 outlines the LCS model and the methods to solve it; a complete derivation of the formulation and solutions outlined in this section is found in Supporting Information "S1 Text". Section, equation, and figure numbers from S1 Text are prefixed by an "S". Section 3 shows the results; and the last section (Section 4) first summarizes the results and then discusses their implications and limitations.

2 Methods: Idealized linear model

This section outlines the linear model and its solutions that will be shown in Section 3. Details are found in Sections S1.2 to S1.4 in S1 Text.

We calculate the 4-d response of an idealized ocean (Section S1.2 in S1 Text) to an idealized model TC (Section S1.4 in S1 Text) on an f plane in an infinite domain with a constant depth $D = 4000$ m. We linearize the primitive equations around a horizontally uniform stratification with no motion [e.g., 13]. The result is the set of 4-d equations (S3) in S1 Text. The set is slightly unusual in that it includes horizontal gradients of atmospheric pressure. For simplicity, we assume a constant buoyancy frequency of $N = 0.002\ \mathrm{s}^{-1}$; this value is chosen so that the gravity-wave speed for the first baroclinic mode, $c_1 \approx 2.5$ m/s (see S1 Table in S1 Text), is reasonable [14]. The TC is assumed to be axisymmetric and have an smooth empirical radial profile of pressure anomaly and tangential winds (Section S1.4 in S1 Text). The TC is also

assumed to move eastward at a constant speed of C_{tc} = 8 m; this value is chosen because it is within the typical range [6] and relatively well satisfies the inequality that $c_1^2 \ll C_{tc}^2$, which helps our anlysis (see Section 3). It is also not too fast: the faster the TC is, the finer the zonal grid spacing needs to be (Section S1.2.4 in S1 Text).

Elements missing from our model include nonlinearity, a more realistic stratification, lateral boundary, bottom topography, and mixing and friction. An axisymmetric TC moving at a constant speed of 8 m/s is also an idealization. We discuss consequences and limitations of these idealizations in Section 4.2.3. Dependency of the solution to the TC speed is discussed in Section 4.2.2.

To solve the set of 4-d equations, we expand the dependent variables in vertical modes [e.g., 13, 15]. In this expansion, we include the barotropic mode ($n = 0$), whose vertical profile and gravity-wave speed are obtained from the free-surface modes, (S4) and (S5) in S1 Text, following [16], whereas we still use the rigid-lid modes as the impacts of free surface on the baroclinic modes ($n \geq 1$) are very minor (Section S1.2.6 in S1 Text).

The coefficients of the expansion, all a function of (x, y, t) for each mode number n, form a reduced-gravity model (RGM; Eq. S8 in S1 Text) forced by contributions from atmospheric pressure and from wind stress. The strength of contribution to each mode is expressed by a "coupling coefficient", which is determined by the vertical profiles of the mode functions and the mixed layer thickness. It turns out that the contribution of atmospheric pressure on the baroclinic modes are negligible [7, also apparent from our Eq. S8 in S1 Text] and therefore only the barotropic response is considered to atmospheric pressure, whereas wind stress strongly forces baroclinic modes.

We then solve the RGM of each mode numerically and superpose the solutions to obtain the 4-d flow field. We sum up to mode 20. The numerical method consists of regular finite differencing. See Section S1.2.4 in S1 Text for details.

One advantage of this approach is that one can get insights from the RGM to understand the behavior of the 4-d flow field as a superposition of the RGMs [e.g., 17]. An important result from previous studies is that the stationary response of the RGM, separately to the wind stress and to pressure anomaly of a moving TC, is a solution to

$$(\nabla^2 - \gamma^2/c_n^2 - \alpha_n^2)(w_n/D) = a_n(f/c_n^2)\mathrm{curl}\,\tau/\rho_o, \tag{1}$$

$$(\nabla^2 - \gamma^2/c_n^2 - \alpha_n^2)\pi_n = -a_n^a \nabla^2 \pi_a \tag{2}$$

on the coordinate system which is moving with the TC, where $\gamma \equiv -C_{tc}\partial_x$. The wind stress and pressure anomaly of the TC are assumed to be steady ($\partial_t = 0$) in this coordinate system. Unfamiliar symbols are defined as follows: $w_n(x, y)$ is the coefficient of expansion such that $w(x, y, z, t) = \sum_{n=0}^{\infty} w_n(x, y, t)\Psi_n(z)$; ρ_o is a mean sea-water density; $\pi \equiv p'/\rho_o$ and $\pi(x, y, z, t) = \sum_{n=0}^{\infty} \pi_n(x, y, t)\psi_n(z)$; $\pi_a(x, y, t) = p_a/\rho_o$ is the atmospheric pressure anomaly divided by ρ_o; c_n is the gravity-wave speed of mode n; $\alpha_n \equiv |f|/c_n$ is the inverse of the deformation radius; and a_n and a_n^a are the coupling coefficients for wind stress and atmospheric pressure. Eqs (1) and (2) are reproductions of Eqs. (S22) and (S23) in S1 Text and their derivations are found in Sections S1.3.2 and S1.3.3 in S1 Text. Shay *et al.* [12] show essentially the same expression for the wind stress response whereas Geisler [7] derives equivalent expressions from a two-layer model for both wind stress and atmospheric pressure.

To help understand the barotropic ($n = 0$) solution, we also solve (1) and (2) numerically. The numerical method is described in Section S1.3.5 in S1 Text.

Green's functions of the operator on the left-hand side are also known [7], which we utilize to interpret our numerical solutions to the RGM. Moreover, an analytic solution to (1) can be

written down as a convolution integral between the wind curl and the Green's function (Eq. S28) in S1 Text. Although unfortunately this integral cannot be carried out analytically for the given model TC, it can be relatively easily evaluated numerically for baroclinic modes because the baroclinic Green's function is benign (Section S1.3.4 in S1 Text).

In the *Results* section (Section 3), we first discuss each vertical mode separately. To give a sense of the size of contribution from each mode to the total 4-d field, each RGM field we show has the same physical dimension as the corresponding 4-d field. For simplicity, however, we set the wind-coupling coefficient a_n to $1/D$ when showing the RGM results, ignoring the adjusting factor a_n', which is $\mathcal{O}(1)$ (Eq. S8) in S1 Text. This factor is put back in when constructing the final 4-d field. Also note that even though $\psi_n(z)$ are normalized to have $\mathcal{O}(1)$ non-dimensional amplitudes for all modes, $\Psi_n(z)$'s amplitudes are $\mathcal{O}(1)$ only for small n (Eqs. S20) in S1 Text.

3 Results

3.1 Vertical velocity in an OGCM

In this subsection, we show an example of a vertical-velocity field associated with one tropical cyclone in our high-resolution ocean general circulation model (OGCM). This model and the method of analysis are described in Section S1.1 in S1 Text. We do *not* claim that this vertical-velocity field is universal or even typical. This small "result" is presented just as an additional "motivation" to our main analysis of the idealized LCS model.

Fig 2 plots a composite of vertical velocity in the OGCM following the center of typhoon 1420 (Typhoon No. 20 of the year 2014). This TC moved approximately in the N40°E direction. Before the time shown in Fig 2A, the TC was moving at a relatively constant speed of $\sim$5 m/s and suddenly speeds up about that time to 10–40 m/s (not shown). The central pressure is about 985 hPa in Fig 2A.

In the y-z section, the vertical velocity peaks somewhat behind the center of the TC. Its vertical profile is interesting. Since the ocean depth is generally 5000–6000 m in this region, the composite values below 5000 m are not reliable. The vertical velocity is nearly zero around 5000 m, increases linearly upwards, peaks at about 700 m, and decays towards the surface. Although this is not visible in the plot, at the surface the velocity is weakly negative, on the order of 10^{-6}–10^{-5} m/s behind the center of the TC up to $y = -2^\circ$.

Upwelling associated with TCs is a well known feature. The shift of its position behind the TC may be interpreted as the quarter phase delay of the near-inertial response (see Introduction). But why does it have to take this cleanly linear profile at depth? These features are common to one or two of the other several typhoons we have sampled (not shown) but they are by no means universal. We will discuss this issue later in Section 4.2.1.

3.2 Barotropic response

3.2.1 Response to ∇p_a. First let us look at the barotropic ($n = 0$) response of the idealized model to the pressure anomaly of the moving TC. For an equilibrium solution following the moving TC, where $\gamma = -C_{tc}\partial_x$, Eq (2) gives

$$[\nabla^2 - (C_{tc}/c_0)^2\partial_x^2 - \alpha_0^2]\pi_0 = -a_0^a\nabla^2\pi_a$$
$$\Rightarrow \nabla^2\pi_0 \approx -\nabla^2\pi_a$$

because $C_{tc}^2 \ll c_0^2$, $L^2 \ll \alpha_0^{-2}$, and $a_0^a = 1$ (note Eq. (S8) in S1 Text, $c_0 = \sqrt{gD}$, and $\psi_0(0) = 1$ for the last equality). Here L is the characteristic scale of horizontal variation in π_a, which is $\mathcal{O}(100\text{km})$ according to S1 Fig in S1 Text, whereas $\alpha_0^{-1} \approx 2900$ km is the barotropic radius of

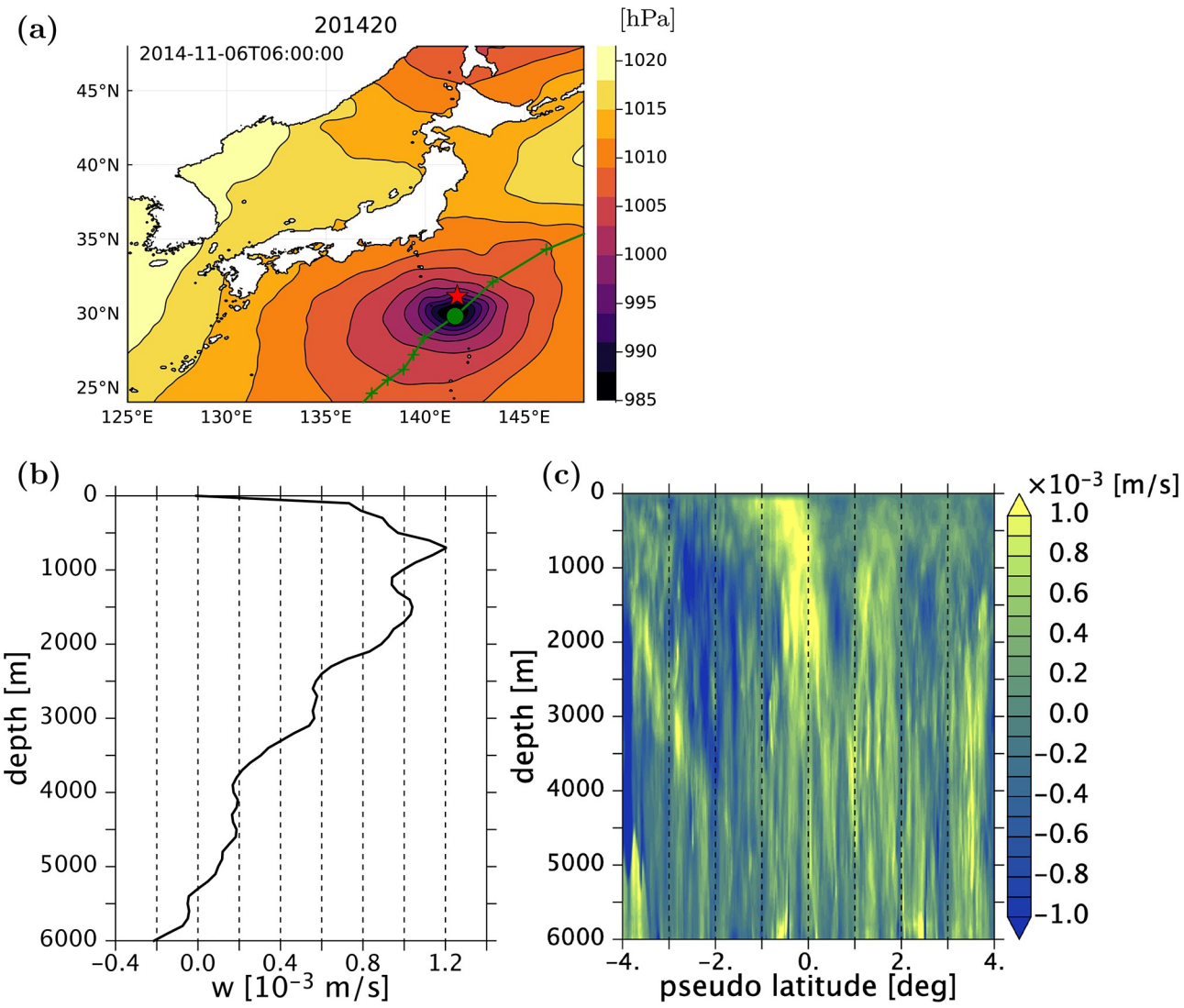

Fig 2. **(A)** Sea level pressure (p_a, hPa) at 2014-11-06T06:00:00Z and the track of typhoon 1420 (No. 20 of the year 2014). The green circle is the estimated center of the TC at the time of the pressure map and the green crosses are the estimated positions at a 6-hr interval. **(B)** Composite vertical velocity averaged over $y = -0.3^\circ$ to $y = 0^\circ$ in TC-centered pseudo latitude for the OGCM (Section S1.1.2 in S1 Text) following the center of the TC (Section S1.1.3 in S1 Text). **(C)** Composite vertical velocity section.

https://doi.org/10.1371/journal.pclm.0000376.g002

deformation. Considering that both π_a and π_0 vanish at infinity and that only the gradients of π_a enter the basic equations (S3) in S1 Text, we conclude

$$\pi_0 \approx -\pi_a + \text{const.}$$

That is indeed the case as shown in Fig 3: The upper panels plot $-\pi_a$ + const. and π_0 and the two curves nearly coincide; the difference between the two fields are very small (lower panel). Moreover, since $\nabla\pi + \nabla\pi_a \approx 0$, u and v are almost zero (see Eqs. S8 in S1 Text) for the equilibrium response.

Baroclinic modes are negligible. For example, we have run the mode 1 RGM. The maximum amplitude of $p_1' = \rho_o \pi_1$ *would* be 4.8 hPa (not shown) *if* the pressure coupling coefficient, a_1^a, *were* as large as a_0^a. Even this hypothetical amplitude is significantly smaller than that

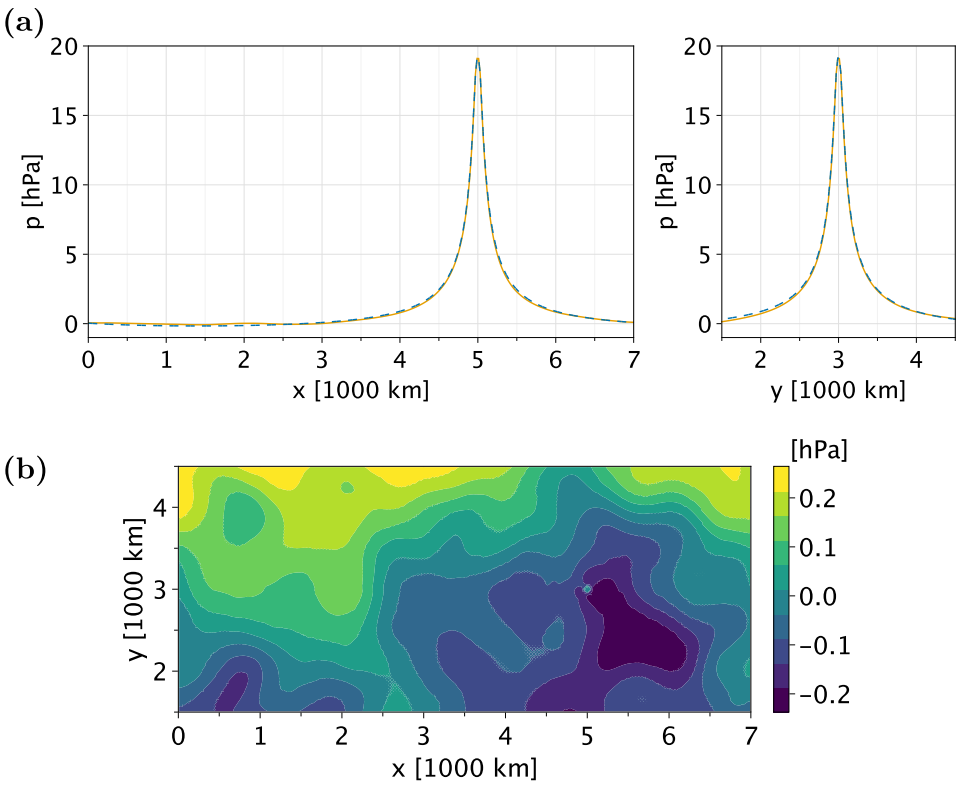

Fig 3. p_a and $\rho_o\pi_0$; the former is the pressure anomaly of the TC and the latter is a temporal average of the pressure response of the $n = 0$ RGM to p_a; $\rho_o\pi_0$ is the temporal average in the moving coordinates over the last 3 d of the integration to suppress gravity waves. The center of the TC is set at (x, y) = (5000 km, 3000 km) in the moving coordinates. The pressure anomaly is a sum of three TC instances 7000 km apart in the x direction to account for the zonal cyclicity of the computational domain. See S1 Text. But the result is not much different if only one instance is used (not shown) because the zonal width 7000 km is significantly larger than the zonal scale of the TC. **(A)** Zonal and meridional sections of $-p_a$ + const. (blue dashed) and $\rho_o\pi_0$ (orange solid) across the center of the TC, but the two curves are so close to each other that they almost coincide. p_a is shifted by the constant value 19.1hPa so that the curves coincide. See S1 Text. **(B)** $\rho_o\pi_0 + p_a$ − const., showing the residual.

https://doi.org/10.1371/journal.pclm.0000376.g003

of p'_0 (Fig 3). It is actually much smaller because

$$a_1^a = \frac{H_1}{D}\psi_1(0) = \frac{c_1^2}{c_0^2}\psi_1(0) \approx 0.0002$$

whereas $a_0^a = 1$. (See Eqs. (S8) and S1 Table in S1 Text and note that $\psi_1(0) = \sqrt{2}$ according to Section S1.2.6 in S1 Text). The actual amplitude is therefore like $4.8 \times 0.0002 \approx 0.001$ hPa for the first baroclinic mode.

With neglect of baroclinic modes, the 3-d distribution of the barotropic pressure is $\pi_0(x, y)$ $\psi_0(z)$, but since $\psi_0(z) = 1$, the anomalous pressure is, at all depth,

$$p = p_a + p' = p_a + (-p_a + \text{const.}) = \text{const.},$$

which is uniform in space (See Eq. S2c in S1 Text). How uniform it is is shown in Fig 3B, which plots the residual:$p' + p_a$ − const. The size of the residual is $\sim$0.2 hPa or less. The cause of this residual is not clear. It may be due to the gravity waves which may still remain after the temporal average because the data interval, 12 500 s, is not frequent enough or because the

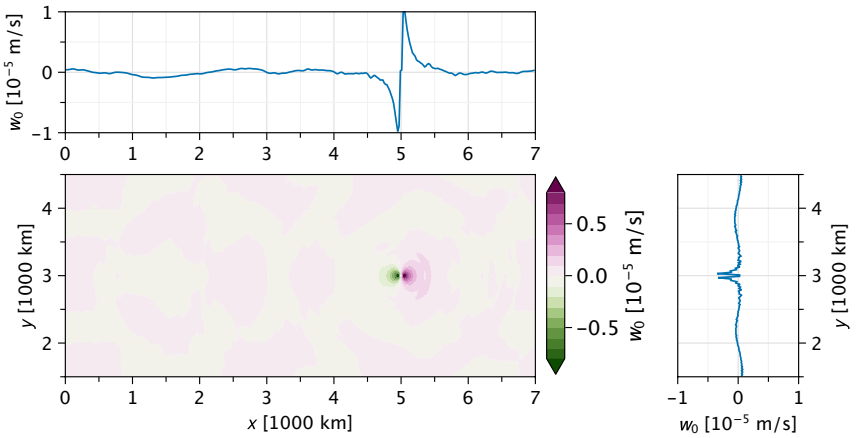

Fig 4. w_0 of the $n = 0$ RGM forced by p_a; average over the last 3 d of the integration to suppress gravity waves.

https://doi.org/10.1371/journal.pclm.0000376.g004

averaging period is not long enough; or it may be due to the approximation that led to the conclusion that $\nabla^2\pi_0 \approx -\nabla^2\pi_a$.

Fig 4 shows the w response. (Despite the 3-day average, it includes low-amplitude small-scale noise, which is likely due to the weakness of any dissipation in the numerical model. See Section S1.2.4 in S1 Text). Equations (S8f) and (S8g) in S1 Text give, on the stationary coordinates,

$$w_0 = \frac{D}{c_0^2}\partial_t\pi_0 = \frac{D}{gD}\partial_t(g\eta_0) = \partial_t\eta_0,$$

because $c_0 = \sqrt{gD}$ and $\pi_0 = g\eta_0$ (Eq S8g) in S1 Text. In the equilibrium state on the moving coordinate system, therefore,

$$w_0 = -C_{tc}\partial_x\eta_0 = C_{tc}\partial_x p_a/(g\rho_o).$$

On the front side of the TC, sea level is raised by the low atmospheric pressure ($\partial_x\eta_0 < 0$ and $\partial_x p_a > 0$), which requires upward vertical velocity $w_0 = -C_{tc}\partial_x\eta_0 > 0$; after the TC center passes, the sea level returns to its original value by the downward vertical velocity behind the TC center. The horizontal scale of the pressure core of the model TC is $L \sim 200$ km and the pressure drop is ~ 10 hPa (S1 Fig in S1 Text), the latter corresponding to a sea level rise of $\Delta\eta = \Delta p/(g\rho_o) \approx 0.1$ m. Therefore, $w \sim \Delta\eta C_{tc}/L \sim 0.4 \times 10^{-5}$ m/s, consistent with Fig 4.

The vertical profile of this vertical velocity is linear: $\Psi_0(z) = z/D + 1$, where $\Psi_0(z = 0) = 1$. The magnitude of the vertical velocity is, therefore, w_0 at the surface, which is $\mathcal{O}(1 \times 10^{-5}\mathrm{m/s})$. The horizontal velocity (not shown) is vertically uniform (because $\psi_0(z) = 1 = \text{const.}$) and $\mathcal{O}(10^{-4}\mathrm{m/s})$.

It is concluded that at the equilibrium, the pressure anomaly of the TC does not induce any significant disturbance to the ocean, except that sea level rises to cancel out the atmospheric pressure anomaly ($\eta = \eta_0 = \pi_0/g = -\pi_a/g$) and except for the associated vertical velocity to supply for the sea level rise and fall on the front and rear sides of the TC center. This state is often called "isostasy". This property always holds for TCs because they are not nearly as fast as barotropic gravity waves and their core size is much smaller than the barotropic deformation radius.

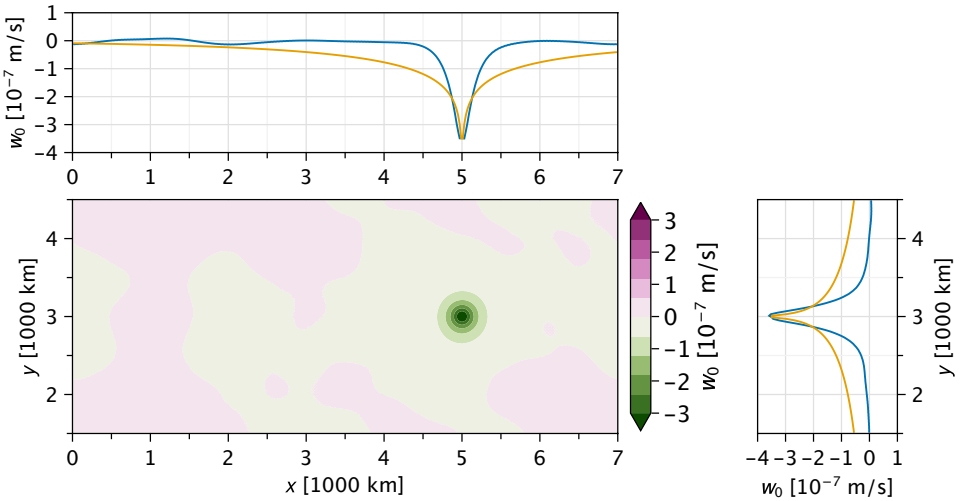

Fig 5. The distribution of w_0 from the mode-0 RGM forced by winds at the end of the integration; zonal and meridional sections across the center of the TC. The orange curve is the analytic impulse response to a delta-function forcing at the center of the TC (Green's function; Eq. S25 in S1 Text); its amplitude is adjusted so that the peak visually agrees with that of w_0, which is fine for a qualitative comparison like this. See Section S1.3.6 in S1 Text for a discussion about the amplitude.

https://doi.org/10.1371/journal.pclm.0000376.g005

3.2.2 Response to curl τ. The barotropic response to a delta-function curl τ is described by [7]. Such a response is often called the "unit impulse response" or the "Green's function". Here, we extend his/her results to a more realistic wind-curl distribution.

Fig 5 shows the w_0 field of the barotropic response to the wind stress of the model TC. As can be inferred from the results of [7], the w_0 field is very nearly circular because curl τ is circular. Anisotropy results only from the anisotropic Laplacian (Eq. (S22) in S1 Text) $(1 - C_{\mathrm{tc}}^2/c^2)\partial_x^2 + \partial_y^2$ but this anisotropy is negligible for the barotropic mode because $C_{\mathrm{tc}}^2/c_0^2 \ll 1$.

Since curl τ is concentrated near the center of TC (S1 Fig in S1 Text), one would suspect that the impulse response would be an excellent solution. It is therefore interesting that the w_0 solution (blue curves) spreads much less than the impulse response (orange curves). Fig 6 compares the impulse response with the actual distribution of w_0. This time w_0 has been

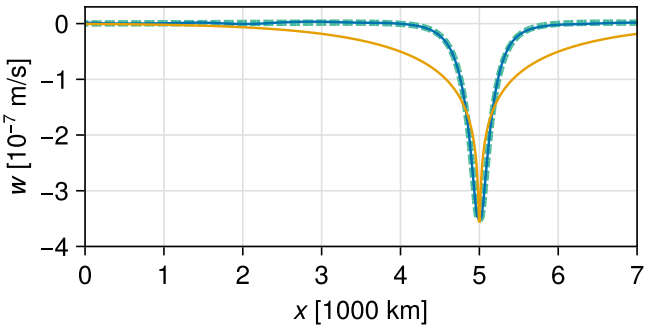

Fig 6. Distribution of w_0 along y = 3000 km from the wind-driven RGM solution. The solid blue curve is the same as that in the top left panel of Fig 5 except that this version is a temporal average over the last three days to suppress gravity waves. The orange curve is different: this time, it is a numerical solution to the "w-equation" (1) forced by a delta-function-like wind curl; its amplitude is adjusted so that the peak visually agrees with that of w_0. The thick dashed green curve is the numerical solution to the w-equation forced by the curl of the same wind stress as forces the RGM.

https://doi.org/10.1371/journal.pclm.0000376.g006

temporary averaged to suppress gravity waves. Also plotted is a numerical solution to the "w-equation" (1) forced by the curl of the same wind stress as forces the RGM. (The numerical method is described in Section S1.3.5 in S1 Text). This solution is plotted with the thick dashed green curve, which agrees well with the RGM solution (blue curve). In contrast, the orange curve is the numerical solution to the w-equation forced by a delta-function-like curl: curl τ = const. within a 20 × 20 km square centered at the center of the TC and curl $\tau = 0$ outside. The solution is then scaled in such a way that its peak visually agrees with the peak of w_0.

Solutions to the w-equation can be viewed as a steady solution to the virtual "heat-conduction equation" (S29) in S1 Text, where positive wind curl is analogous to "heat source" and $-w$ is analogous to "temperature". The "heat" provided by the forcing is laterally diffused by the Laplacian term and gradually lost by the "radiative cooling" $-\alpha^2 \cdot (-w)$. Since "cooling" is weak, that is, the radius of deformation (α^{-1}) is large, the anomaly spreads broadly.

The difference between the realistic w_0 response and the impulse response must therefore be attributable to the negative wind curl, "heat sink", outside the TC core (S1 Fig in S1 Text). It is therefore the negative wind curl outside the TC core which limits the horizontal extent of w. Although weak in magnitude, the negative curl is effective (in absorbing "heat") because it covers an area much larger than the area of positive curl. A region of negative curl is an integral part of a TC because its wind decays (or must decay) fast outside the TC core. See the discussion of S1 Fig in S1 Text.

As discussed for the p_a response in the previous subsection, the pressure, and equivalently sea-level, response is the zonal integration of w (Fig 7). The pressure starts to drop ∼400 km before the TC center and reaches its negative peak ∼400 km behind the TC center, corresponding to the zonal scale of w_0 (Fig 7). Since the speed of this TC is 8 m/s, these corresponds to ∼0.7 d before and after the passage of the TC center in the stationary system. The lateral extent is the same as that of w_0, that is, $\Delta y \sim \pm 400$ km. In the wake of the TC, the low pressure stays at its peak value. Geostrophic circulation is left behind; $(u, v) \approx g(-\eta_y, \eta_x)/f$ is a very good approximation (not shown). The velocity is vertically uniform (because $\psi_0(z) = 1$) and its amplitude is less than 0.75 cm/s (not shown). The horizontal scale of the pressure anomaly and the associated velocity anomaly are therefore ultimately determined by the radial structure of the wind curl of the TC.

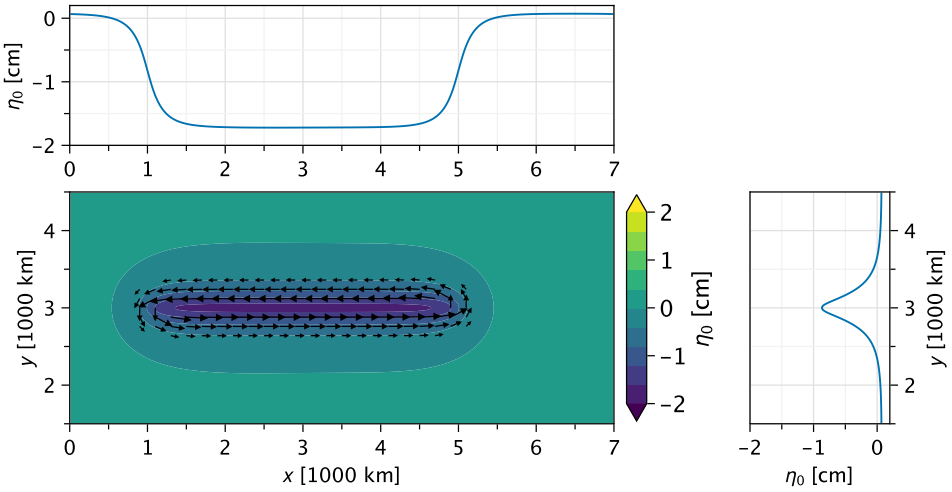

Fig 7. The distribution of η_0 from the mode-0 RGM at the end of the integration; zonal and meridional sections across the center of the TC. Since $p_0' \equiv \rho_o \pi_0 = g\rho_o \eta_0$, of sea level anomaly corresponds to 1 hPa of pressure anomaly (note that $\psi_0(0) = 1$). The arrows indicate the horizontal velocity (in the stationary coordinates).

https://doi.org/10.1371/journal.pclm.0000376.g007

3.3 Baroclinic response

Next we look at baroclinic modes. As stated above, the baroclinic response to p_a is extremely weak, and here we focus on response to curl τ.

3.3.1 Mode 1: *w*. Fig 8 plots $-w_1$ from the $n = 1$ RGM and from the numerical evaluation of the analytic solution (Section S1.3.4 in S1 Text) to (1). The unfortunate consequence of the sign convention ($\psi(0) > 0$) and ψ's relation with Ψ (Eqs. S6) in S1 Text is that $\Psi_n(z) < 0$ near the surface for all $n \geq 1$; for this reason, $w_n < 0$ means upwelling near the surface.

As is well known, a typical TC leaves a train of near inertial oscillation behind, which is because $C_{tc} > c_1$ for a typical TC as explained in the following. The orange curve is a plot of the Green's function centered at $(\tilde{x}, \tilde{y})$ of the w-equation:

$$G(x - \tilde{x}, y - \tilde{y}) = -\frac{\alpha^2}{2\sqrt{C_{tc}^2/c^2 - 1}} J_0(\sqrt{x^{*2} - y^{*2}})\theta(-x^* - |y^*|), \tag{3}$$

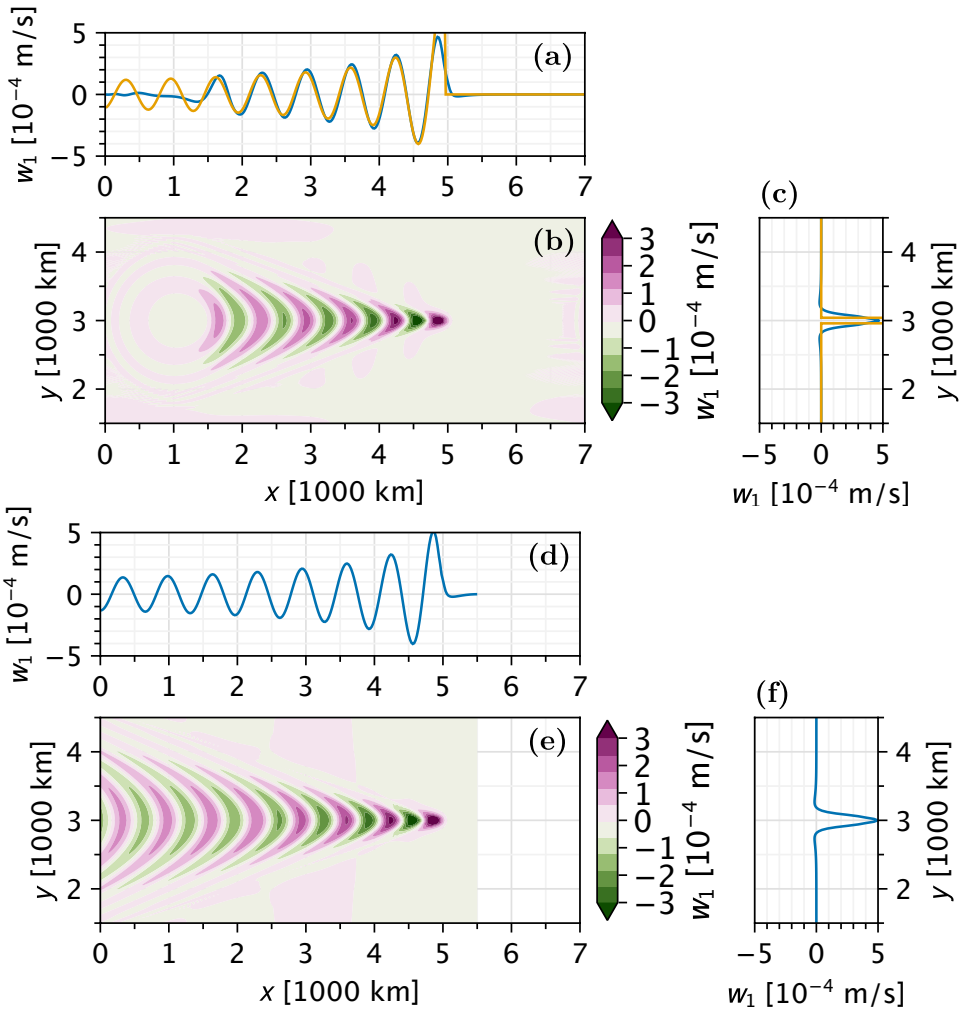

Fig 8. Vertical velocity $-w_1$ of RGM mode 1 at the end of the integration **(A) (B) (C)** and the numerically evaluated analytic solution **(D) (E) (F)**. See Eq. (S28) in S1 Text for the latter solution. The zonal section goes through the center of the TC ($y = 3000$ km) whereas the meridional section is $x = 2850$ km, where the peak of w_1 is. The impulse response (Green's function, orange curves) is shifted westward by 30 km and its amplitude is adjusted, both in such a way that the curve visually agrees with the w_1 curve.

https://doi.org/10.1371/journal.pclm.0000376.g008

where J_0 is the Bessel function of the first kind of order 0 and

$$x^* \equiv \frac{\alpha\,(x-\tilde{x})}{\sqrt{C_{\rm tc}^2/c^2-1}}, \quad y^* \equiv \alpha\,(y-\tilde{y}) \tag{4}$$

[7, and see Eq. (S26) in S1 Text of the present paper]. The actual solution is a convolution integral between the Green's function and the wind-stress curl (Eq. S28) in S1 Text, but since the strong positive wind-stress curl is concentrated in a circle of a radius $\sim$100 km (S1 Fig in S1 Text) the Green's function is a fairly good representation of the actual solution.

The meridional extent of the solution scales as α^{-1} (= c/f). The wavelength of $J_0(r^*)$ is very nearly 2π near $r^* = 0$ (not shown) and therefore the zonal wavelength at $y^* = 0$ near $x^* = 0$ is

$$\lambda_n = 2\pi\frac{\sqrt{C_{\rm tc}^2/c_n^2-1}}{\alpha_n} = 2\pi\frac{\sqrt{C_{\rm tc}^2-c_n^2}}{f}, \tag{5}$$

which slowly increases as c_n decreases for higher modes. For mode 1, where $c_1 \approx 2.55$ m/s, $\lambda_1 \approx 655$ km. But, because usually $c^2 \ll C_{\rm tc}^2$ for all baroclinic modes,

$$\lambda \approx 2\pi C_{\rm tc}/f \quad \text{and} \quad \lambda < 2\pi C_{\rm tc}/f,$$

and the structure of the solution depends only weakly on c in the x direction and the zonal wavelength is mainly determined by the speed of the TC. In the stationary coordinate system, because this wave train moves eastward at the speed of $C_{\rm tc}$, the angular frequency of the oscillation is $\omega = 2\pi C_{\rm tc}/\lambda \approx f$ and $\omega > f$, that is, this oscillation is near-inertial.

An obvious difference between the Green's function and the actual solution (Fig 8A) is that the former extends westward indefinitely because it assumes a steady state in the moving coordinates. The system can propagate disturbance no faster than c and this explains the nearly perfect circle centered at (x, y) = (1000 km, 3000 km) (Fig 8B), where the TC initially was. Also, the meridional extent of w_1 at its peak is much narrower in the Green's function (the orange curve in Fig 8C). This is again because the signal from the forcing, which is a delta function for the impulse response, cannot propagate faster than c. Moreover, to obtain a good match with the actual solution, the Green's function has to be shifted westward by 30 km (the orange curve in Fig 8A).

These discrepancies indicate that the position of the peak in w_1 behind the TC and its meridional structure need to be explained by the convolution integral between the actual distribution of curl τ and G. Fig 8D to 8F show a numerical evaluation of the convolution integral, which we sometimes call the "analytic" solution for convenience. This solution is quantitatively very similar to the RGM solution. Fig 9 compares the two solutions in detail. The match is nearly perfect in the zonal section (Fig 9B) except that the first peak is somewhat larger in the "analytic" solution. The wavelength of the Green's function is slightly longer than that of the actual solution (Fig 8A); this difference also comes from the difference between the Green's function itself and the convolution. Since the actual solution is a westward integration of wind-stress curl times the Green's function (Eq. S28) in S1 Text, the peak response in w_n is a westward accumulation of forcing curl τ and the peak comes west of the TC center, whereas the peak of the Green's function itself is located right at the TC center. This is the reason for the 30km westward shift applied to the orange curve in Fig 8A.

The meridional structure at the first peak (Fig 9C) also agrees well between the two solutions. The Green's function shows a clear causal relation (Eq. (S26) in S1 Text): No response

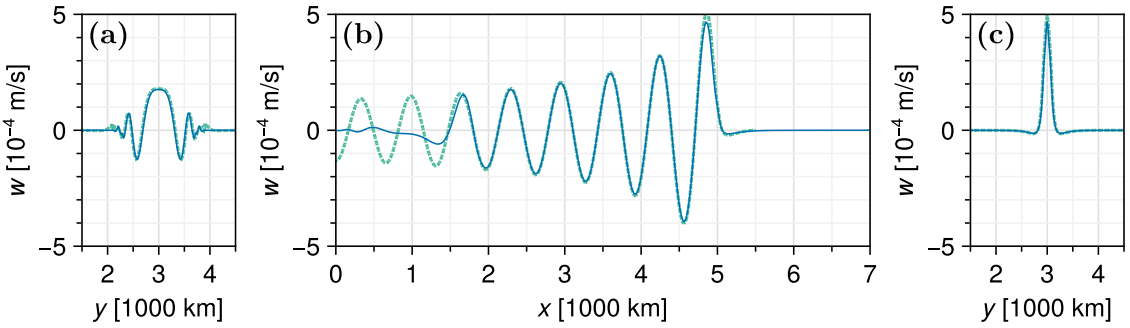

Fig 9. Vertical velocity $-w_1$ of RGM mode 1 (a) at $x = 2290$ km, where the 9th peak is, (b) across the center of TC, $y = 3000$ km, and (c) at $x = 4850$ km, where the 1th peak is. The solid blue curve is the numerical solution to the RGM at the end of integration, and the thicker dashed green curve is the numerically evaluated analytic solution to the w equation (Eq 1; see Section S1.3.4 in S1 Text).

https://doi.org/10.1371/journal.pclm.0000376.g009

shows up outside the causal triangle $x^* < y^* < -x^*$ with $x^* < 0$. In dimensional variables,

$$-\frac{c}{C_{\mathrm{tc}}}(\tilde{x} - x) < (y - \tilde{y}) < \frac{c}{C_{\mathrm{tc}}}(\tilde{x} - x) \tag{6}$$

from (4) because $C_{\mathrm{tc}}^2/c^2 \gg 1$ and $\alpha = f/c$. The triangle extends from $(\tilde{x}, \tilde{y})$ westward, northward, and southward. This triangular shape is a natural consequence of the condition that $C_{\mathrm{tc}} > c_n$ [7] but we are not aware whether it has been observed or not. If there are no observational reports, it may be because the near surface response is dominated by higher vertical modes (see Section 3.4 below), for which the meridional spread is narrower (see Section 3.3.3 below).

This is the bound where gravity waves can reach from the delta-function forcing. This is the reason why G has a sharp edge at the triangle. The actual response is smoother because the forcing is smooth but the amplitude of the response rapidly decays outside the triangle which starts from the TC center (Fig 8A and 8C) because the forcing (wind curl) decays rapidly away from the TC core.

The meridional spreading due to gravity waves, as represented by the width of the orange curve in Fig 8C, is narrower than the meridional scale of the wind curl itself and therefore the overall meridional width at this point (150 km behind the TC center) is determined mainly by the meridional scale of the wind curl.

Further west (Fig 9A), the upwelling or downwelling region spreads meridionally by gravity waves but the total response is a superposition of gravity waves generated at various places. (This superposition is what the convolution integral does.) The net result is a wavy pattern that includes small scale features near the edge (Fig 9A). It is interesting that at the poleward edges the "analytic" solution has small but nonzero amplitudes beyond the latitudes where the numerical RGM response vanishes. This may be because the numerical convolution integral must be carried out at a higher horizontal resolution to cancel out these tiny wiggles or because small-scale gravity waves are somewhat slower in the numerical RGM.

3.3.2 Mode 1: Other fields. Fig 10 plots $\eta_1\psi_1(0)$. We include the factor $\psi_1(0)$ to indicate the contribution of the mode to the actual total sea level; see (S7) in S1 Text. As stated for the barotropic mode, $w_n = -C_{\mathrm{tc}}\partial_x\eta_n$ at the equilibrium state on the moving coordinates and therefore the η_n field is proportional to a westward integration of w_n. For this reason, the peaks of η_1 is a quarter phase behind those of w_1. The location of the first minimum pressure (sea level) is therefore determined by both the horizontal size of the strong-curl core of the TC and the

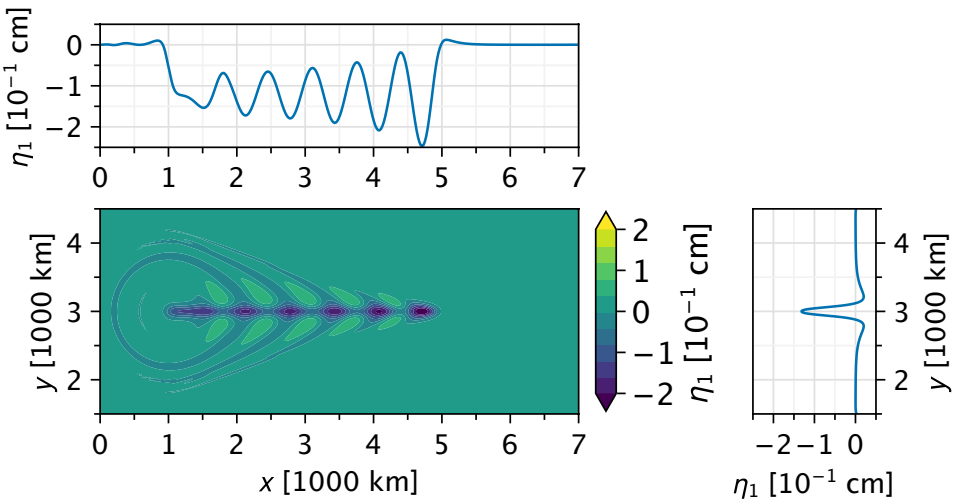

Fig 10. Same as Fig 8 except that this one plots $\eta_1\psi_1(0)$. Note that the meridional section is still where w_1 is at its peak, not η_1.

https://doi.org/10.1371/journal.pclm.0000376.g010

natural wavelength ($2\pi f/C_{tc}$) of the near-inertial oscillation. It is located 300 km behind the TC center, which corresponds to about 10 hr behind in the stationary coordinate system. Interestingly the response of pressure is not only a near-inertial oscillation but also there is a net pressure drop. The size of the average drop is less than 1/10 of the barotropic mode (Fig 7).

Since pressure (π), sea level (η), and buoyancy (b) are tied by $\pi_n = g\eta_n = -Db_n$ for each mode (Eqs. S8e and S8g) in S1 Text, a negative pressure anomaly simultaneously means a negative sea level anomaly and a positive density anomaly near the surface (because $\psi_n(0) > 0$ according to our sign convention). Therefore, pressure anomaly near the surface is negative owing to the lowered sea level despite the positive density anomaly. The density response is shown later for the total 4-d field.

It is not easy to show the velocity field in arrows on the map (10) as it is dominated by eddy-like wave pattern as shown in [3]. Its magnitude is less than 0.8 cm/s (not shown).

3.3.3 Mode 10 and higher. As the mode number increases (that is, as c_n decreases), the triangle of causality (6) shrinks in the meridional direction because c_n/C_{tc} decreases. For mode 10, for example, $c_{10} \simeq 0.25$ m/s and $c_{10}/C_{tc} \simeq 0.03$, which means that even after 5000 km of TC passage the meridional spread of the signal is just ±160 km (Fig 11). As a result, the response to the forcing is dominated by the westward integration of wind curl with the Green's function as in (S28) in S1 Text. That is why the meridional structure of w_{10} near the TC center (Fig 12C) is similar to the meridional structure of wind curl, which has two peaks at $\Delta y \approx \pm 20$ km (S1 Fig in S1 Text).

According to (5), the zonal wavelength near the TC center is approximately 690 km, somewhat longer than 655 km for mode 1. These wavelengths are not inconsistent with the distance between the 1st and 9th peaks in $|w|$ quoted in the captions to Figs 9 and 12, according to which the wavelengths are 695km for mode 10 and 640km for mode 1.

The pressure response again includes a mean drop and is much smaller (Fig 11) than that of mode 1 (Fig 10). The velocity field again takes a form of series of eddies and is smaller than 1 cm/s.

Further reduction in c_n brings about even smaller changes to the response of the mode to wind curl. The meridional spread of signal becomes even narrower and as a result, so does the causal triangle, and the westward convolution integration dominates even more. In other

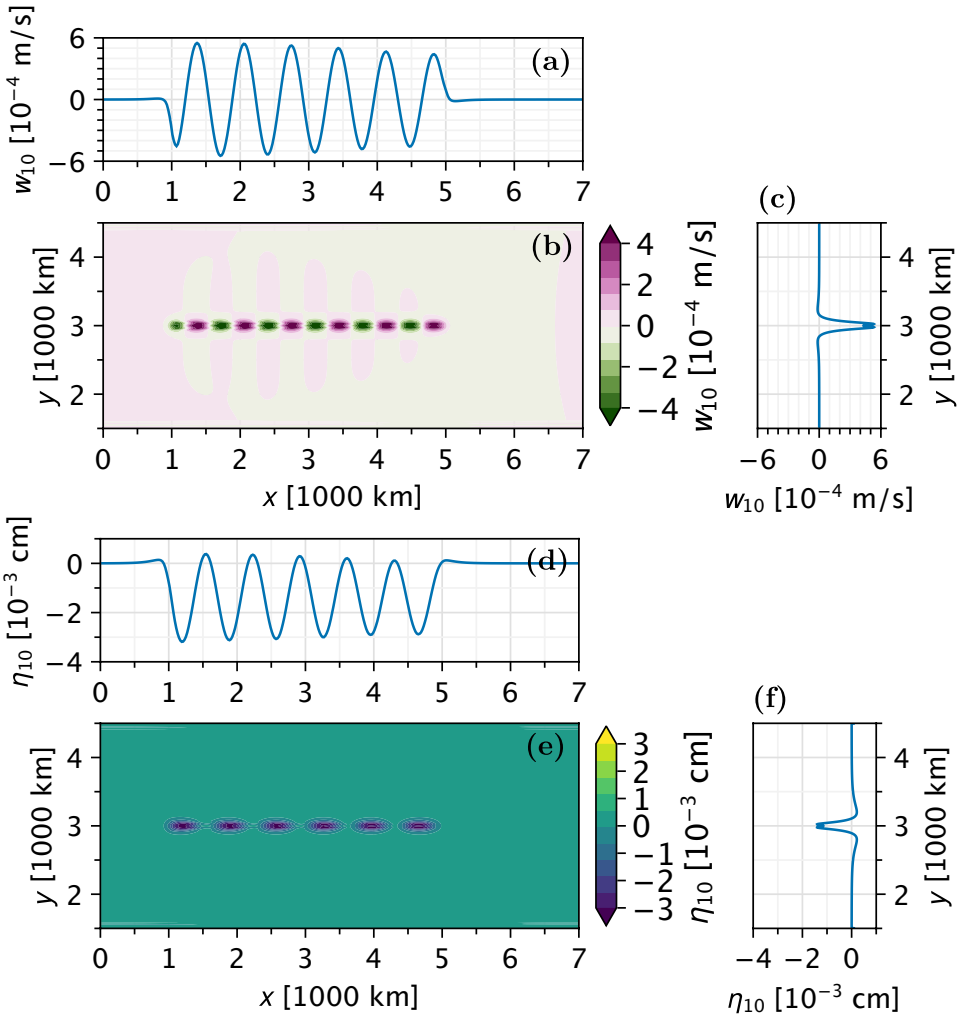

Fig 11. Vertical velocity $-w_{10}$ and sea level $\eta_{10}\psi_{10}(0)$ of RGM mode 10 at the end of the integration. The zonal section goes through the center of the TC (y = 3000 km) whereas the meridional section is 170 km to the west, where the peak of w_{10} is.

https://doi.org/10.1371/journal.pclm.0000376.g011

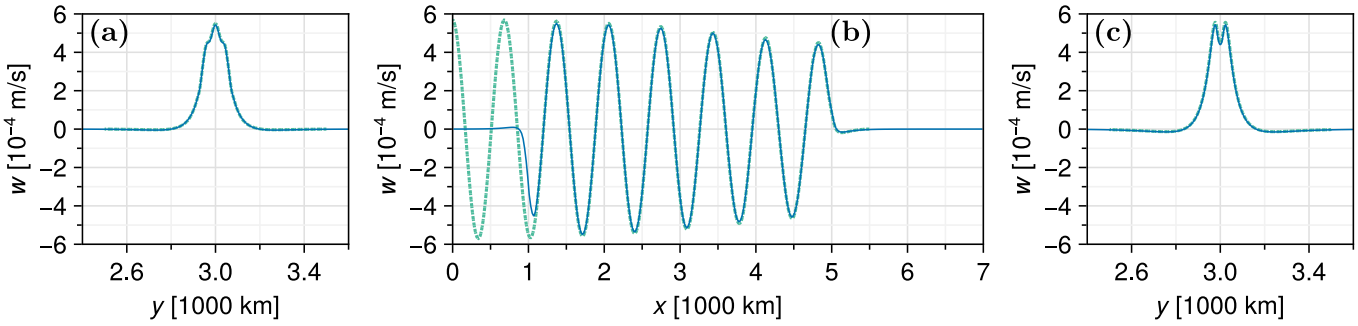

Fig 12. Vertical velocity $-w_{10}$ of RGM mode 10 **(A)** at x = 2050 km, where the 9th peak is, **(B)** across the center of TC, y = 3000 km, and **(C)** at x = 4830 km, where the 1th peak is. The solid blue curve is the numerical solution to the RGM at the end of integration, and the thicker dashed green curve is the numerically evaluated analytic solution to the w equation (Eq 1; see Section S1.3.4 in S1 Text).

https://doi.org/10.1371/journal.pclm.0000376.g012

words, the response of the mode converges as c_n becomes smaller. (If we looked at $x \to -\infty$, the signal always spreads meridionally for all modes, but we are interested in a limited range of x.)

Our numerical RGM solution agrees with the convolution integral at mode 20 (not shown) as well as it does at mode 10 (Fig 12) even though with $c_{20} \approx 0.13$ m/s, the deformation radius $c_{20}/f \approx 1.9$ km is hardly resolved by our meridional grid spacing of 2 km. This result must be because the meridional spread of the solution (as embodied by the Green's function) is negligible and the numerical grid does not need more meridional resolution than for lower modes.

3.4 Three-dimensional structure

The three-dimensional (x, y, z) structure is constructed as a summation of the RGM solution times the vertical structure function (Eq. S7) in S1 Text. For the wind-forced solution, we adjust the amplitude of each RGM solution to reinstate the factor a'_n (Eq. S8) in S1 Text in the summation. For the p_a-forced solution, we just use mode 0 only as the higher modes are negligible (Section 3.2.1).

3.4.1 *w* field. Fig 13 shows the wind-forced 3-d solution at the end of integration. (The p_a-force w is negligibly small as discussed later in Section 3.6.1 and so is ignored here.) At about 150 km behind the TC center, there is a vertical column of strong upwelling, which grows linearly from 0 at the bottom to $\sim 4 \times 10^{-4}$ m/s at $z \approx -250$ m and then decays to 0 at the surface (Fig 13G). This profile is similar to that found in the JCOPE model (Fig 2) except that the depth of the peak appeared more like 700m in the latter. This vertical coherence in the idealized model is because all baroclinic modes have the first peak in w_n approximately here. The vertical structure is a result of constructive interference in the upper ocean and destructive interference at depth between the vertical structure functions $\Psi_n(z)$ of the modes.

Further behind, the phase lines tilt backwards. The zonal wavelength becomes longer as c_n decreases (Eq 5) but the rate of this change slows down as n increases (and λ_n approaches a constant value). For this reason, the vertical alignment of peaks in w_n (Figs 8 and 11) is gradually lost between the lowest modes and the higher modes whereas the coherence between the higher modes mostly remains, and the shallowest peak in w remains at ~ 300 m, which is created by the sum of the higher modes where as the relation of the other, deeper peak(s), which are created by lower modes, to the shallowest peak, keeps shifting (Fig 13E and 13F).

The meridional evolution of the wave train is also explained as a superposition of modes. The meridional spread is obviously faster for lower modes (Eq 6; Figs 8 and 11), and as a result, the outer edges are dominated by a 1st-mode-like structure and variability is found only at mid depths away from the TC track (Fig 13B and 13C).

This 3-d structure should *also* be explainable as a behavior of 3-d inertio-gravity waves because after the passage of the TC, the w disturbance left behind should follow the dispersion relation of internal gravity waves. Although the 3-d disturbance field is a superposition of waves with a wide range of vertical wave numbers and does not render itself to a simple WKB interpretation, at least the propagation of the phase is consistent with the interpretation that this is a kind of *lee wave* response: We have plotted x-t and z-t Hovmöller diagrams at a fixed x behind the center of TC (not shown) and found that the phase propagates upward and forward (positive x), consistent with the regular lee wave [e.g., 18].

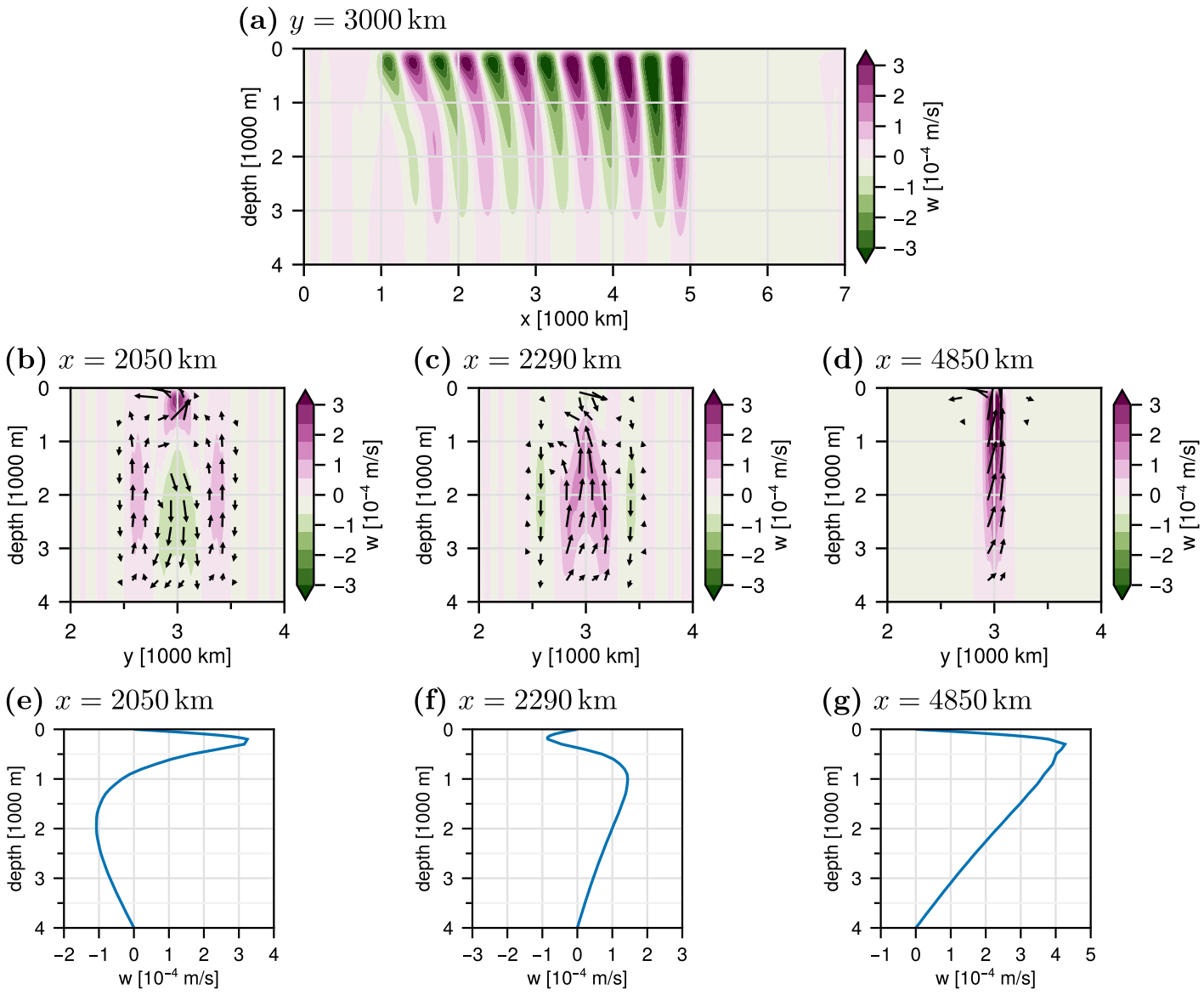

Fig 13. Vertical sections of *w*(*x*, *y*, *z*) forced by winds at the end of integration. The units for the contouring are 10^{-4} m/s. Arrows indicate velocity vectors (*v*, *w*) in each meridional section; velocity is omitted for the zonal section to avoid too much cluttering. The velocity components, *v* and *w*, are scaled in such a way that the arrows are parallel (tangent) to local stream lines, each pointing in the direction of the motion of the local water parcel. The zonal section (A) is through the center of the TC; the meridional sections are where the 9th peak is located for mode 10 (B) and for mode 1 (C) and where the 1st peak is for mode 1 (D); and the vertical profiles (E)(F)(G) are taken at $y = 3000$ km for these three sections. The position of the 1st peak for mode 10 is omitted because it is quite close to that for mode 1.

https://doi.org/10.1371/journal.pclm.0000376.g013

This indicates a downward and forward energy propagation [e.g., 15]. Using the standard dispersion relation [e.g., 15] of internal gravity waves

$$\omega = \left(\frac{N^2(k^2 + l^2) + f^2 m^2}{k^2 + l^2 + m^2} \right)^{1/2},$$

and for the 1st baroclinic mode, which has a vertical wavenumber of $m = \pi/D$ (Eqs. S20) in S1 Text, a zonal wavenumber of $k = 2\pi/\lambda_1 = f/\sqrt{C_{tc}^2 - c_1^2}$ (Eq 5), and a meridional

wavenumber of $l = 2\pi/800$ km from a rough estimate of the half-amplitude meridional width of 400 km (Fig 12), we calculate the group velocities

$$\begin{aligned}(c_g^x, c_g^y, c_g^z) &= (\omega_k, \omega_l, \omega_m) \\ &= \frac{m(N^2 - f^2)}{(k^2 + l^2 + m^2)^2 \omega}(km, lm, -k^2 - l^2) \\ &\approx (0.78, 0.64, -0.015)\ \mathrm{m/s}.\end{aligned}$$

(The horizontal group velocities can be calculated from the standard dispersion relation $\omega^2 = f^2 + c^2(k^2 + l^2)$ of the inertio-gravity wave (Poincaré wave) of the single-mode RGM because $c_1 = ND/\pi = N/m$ for mode 1. This is because the 3-d internal-wave dispersion relation reduces to that of the Poincaré wave in the limit that $k^2 + l^2 \ll m^2$.) Likewise, for mode 10 as another example,

$$(c_g^x, c_g^y, c_g^z) \approx (0.008, 0.007, -1.6 \times 10^{-5})\ \mathrm{m/s}.$$

Morozov & Velarde [19], analyzing observed near-inertial waves generated by a typhoon near Japan, reported that the vertical propagation speed is 1–10 m/hr (2.8×10^{-4}–2.8×10^{-3} m/s). Because the wave pattern is a superposition of vertical modes with a wide range of wavenumbers, the range of the propagation speed is large. One caveat is that our linear model misses the potential trapping of small-scale near-inertial waves owing to the relative vorticity [e.g., 20].

In the coordinate system moving with the TC, energy propagates backwards away from the TC, which corresponds to the typical lee-wave situation, where winds blow over a mountain. When the wave maker is moving, however, the energy propagates toward the wave maker [e.g., 18] in the stationary coordinate system. One interesting difference from typical lee waves is that the TC generates anomaly from the surface to the bottom at once as a column, which is the reason why disturbance shows up near the bottom relatively quickly despite the slow vertical group speed.

It is interesting that the meridional profile (Fig 14B) of w at a shallow depth retains the double peak structure of higher modes (Fig 12C).

3.5 Density field

The vertical structure of ρ' ($= -\rho_o b/g$), as shown in Fig 15, is similar to that of w (Fig 13): like w, the maximum value, $\sim 5 \times 10^{-3}$ kg/m^3, is located at $\sim$200–300 m. The density anomaly is, however, is a westward integration of $N^2 w$ as one can see by replacing ∂_t with $-C_{tc}\partial_x$ in (S3e)

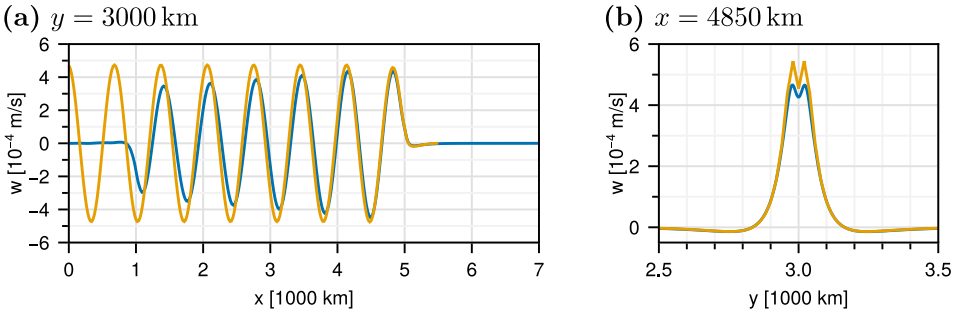

Fig 14. Zonal ($y = 3000$ m) and meridional ($x = 4850$ m) profiles of w (blue) at $z = 300$ m, where w is maximum (see Fig 13G). The latter section is where the first peak in w is. The orange curves are from the analytic solution (S45) in S1 Text of the uniform-density ocean. This point is discussed later.

https://doi.org/10.1371/journal.pclm.0000376.g014

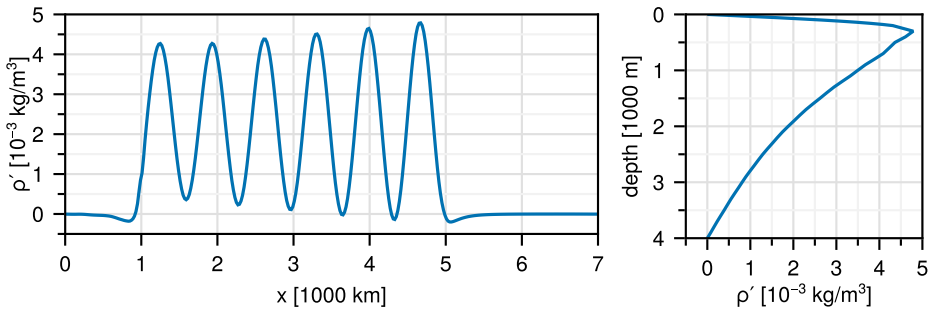

Fig 15. Density anomaly at $y = 3000$ km: zonal profile for $z = 300$ m (left) and vertical profile at for $x = 4670$ km (right).

https://doi.org/10.1371/journal.pclm.0000376.g015

in S1 Text, and the maximum density anomaly is located ($x \approx 4670$ km) a quarter phase behind that of w (Figs 8 and 13). More importantly, positive density anomalies are much stronger than negative ones everywhere and the near-inertial oscillation occurs between zero and the maximum (Fig 15). Since the initial upwelling is the largest (Fig 8), the subsequent near-inertial oscillation does not entirely cancel out the densification. This result is of course consistent with the well known phenomenon that TC-induced upwelling leaves cold water behind (see Introduction).

3.6 Pressure field

Figs 16 and 17 plot the pressure field. The response to p_a is again ignored because it is too small (Fig 3). The dominant response is the barotropic one (Fig 7): p' starts to drop throughout the water column $\sim$400 km ahead of the TC center and the drop is complete $\sim$400 km behind the TC center. The size of this anomaly is about 1.7 hPa (Figs 7 and 17). The meridional scale, $\sim \pm$ 400 km, of the response also comes from the barotropic mode (Figs 7 and 16).

Fig 16E plots only the baroclinic modes, i.e., a superposition of modes 1–20 excluding mode 0. The baroclinic modes generally reinforce the pressure drop near the surface and weakens it near the bottom. This baroclinic structure is a result from the combination of the density anomaly and sea level anomaly: At $z = 0$, where only $\rho_o g\eta$ contributes to the pressure anomaly (Eq. (S2c)) in S1 Text, the lowered sea level (Fig 17A, green curve) provides negative pressure anomalies; at $z = -D$, the positive pressure anomaly due to the positive density anomaly (Fig 15) overwhelms the negative surface pressure anomaly (Fig 17B, green curve).

As a result of this anti-symmetric baroclinic anomaly, after the passage of the TC the surface pressure reaches its first negative maximum $\sim$300 km behind, but the bottom pressure reaches its first negative maximum $\sim 600km$ (Fig 17); these numbers correspond to 10 hr and 20 hr, respectively, of delay after the passage of the TC center.

Even though the baroclinic pressure anomaly vanishes on vertical average (because $\int_{-D}^{0} dz\, \psi_n = 0$ for $n \geq 1$), the maximum amplitude is larger and its vertical extent is smaller near the surface than near the bottom (Fig 16E). As a result, the total pressure anomaly is $\sim$1.4 hPa at the bottom and sometimes exceeds $\sim$2 hPa at the surface, as compared with the barotropic pressure anomaly of $\sim$1.7 hPa (Fig 17).

3.6.1 Sea surface response. Since we include only mode 0 for the p_a-forced solution, the 3-d structure of the p_a-forced w is the 2-d structure of Fig 4 times the vertical structure function $\Psi_0(z) = z/D + 1$ of mode 0. This w field is more than 10 times smaller than that driven by

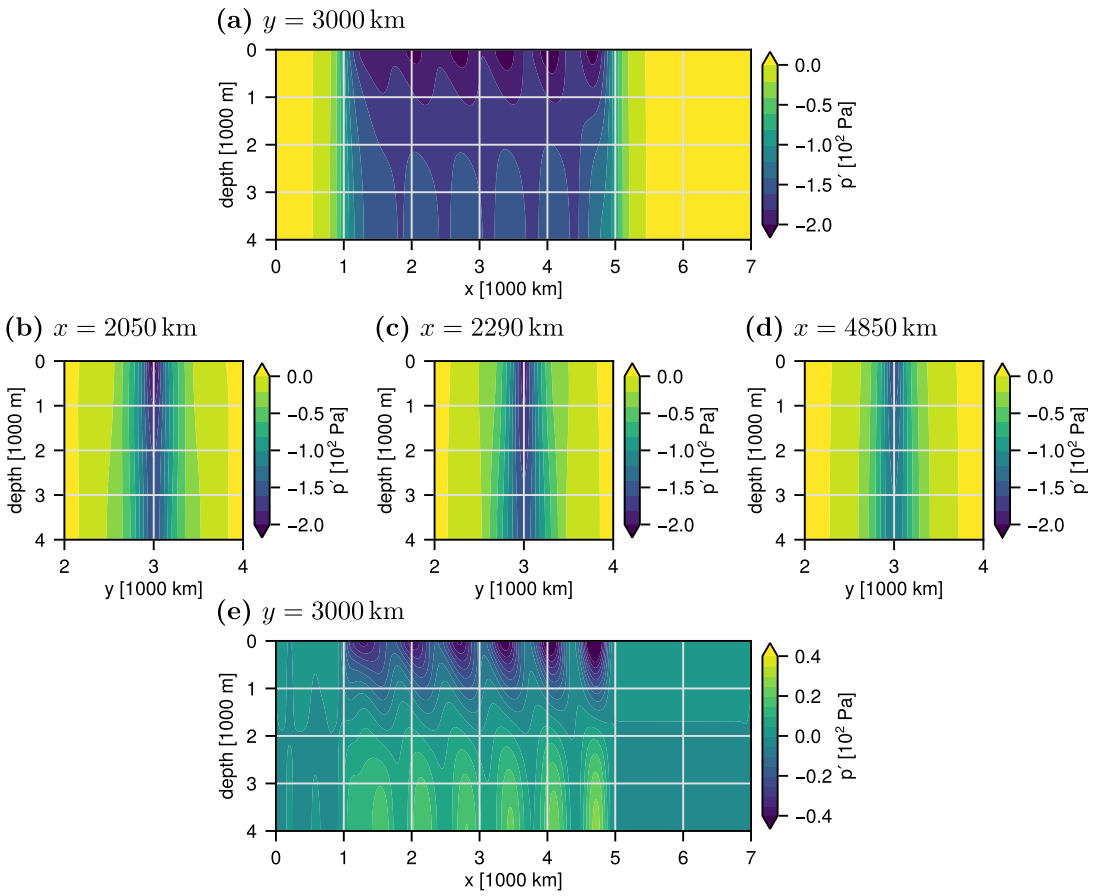

Fig 16. Vertical section of p' forced by winds at the end of the integration. The first four panels plot the total p' whereas Panel E plots the baroclinic component only. Note the color levels: positive values in the total p' are negligibly small and the shading is designed to cover negative values, whereas the shading for the baroclinic p' is balanced and covers a smaller range of values.

https://doi.org/10.1371/journal.pclm.0000376.g016

winds (Figs 8 and 11). We actually tried adding this w field to the wind-driven w above, but the result was visually indistinguishable from that of the wind-forcing-alone solution except very near the sea surface.

Even smaller is the barotropic, wind-driven w. Although too weak to be visible in Fig 13, $w < 0$ at the surface for the wind response. This feature is solely due to the barotropic mode (Fig 5) as $\Psi_0(0) = 1$ and $\Psi_{n>0}(0) = 0$.

In contrast, the sea level anomaly is utterly dominated by p_a forcing (Fig 3). The associated surface pressure anomaly, however, is almost totally canceled by p_a itself (Fig 3) and the sea-level pressure anomaly is dominated by the barotropic response to winds (Fig 17) followed by the baroclinic response.

3.7 Uniform-density ocean

The clean linear profile of w below the mixed layer (Figs 2 and 13) is curious. In this subsection, we consider the response of the same linear ocean (S3) in S1 Text except that density is uniform, that is, $N = 0$, and show that a similar vertical profile of w results. A key equation in

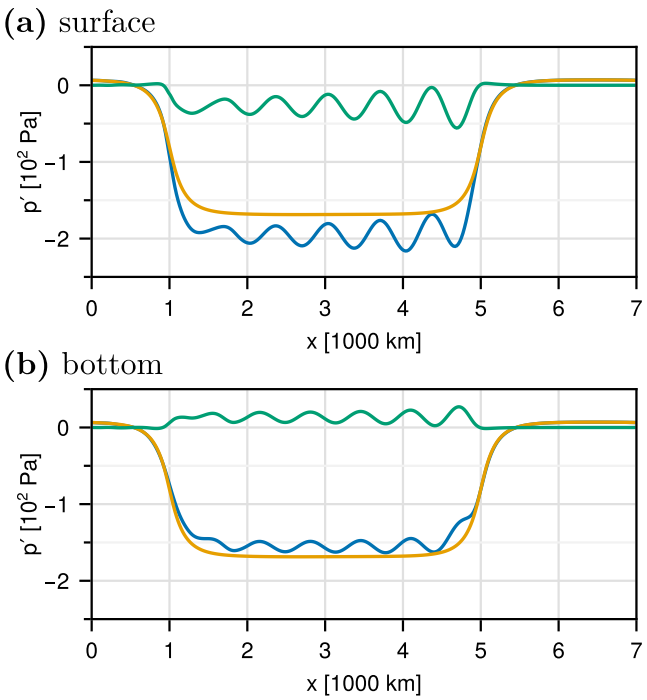

Fig 17. Zontal distribution of pressure anomalies at the sea surface **(A)** and bottom **(B)** behind the TC center (y = 3000 km): total pressure anomaly (blue), barotropic mode (orange), and the sum of the baroclinic modes (green).

https://doi.org/10.1371/journal.pclm.0000376.g017

this discussion is Eq. (S40) in S1 Text; to reproduce it here

$$(\partial_t^2 + f^2) w_{\mathrm{E}} = f \,\mathrm{curl}\, \tau/\rho_{\mathrm{o}}, \tag{7}$$

where w_{E} is the Ekman pumping velocity (positive upward).

3.7.1 Stationary wind curl. The theoretical steady response of a flat-bottom, uniform-density linear ocean to a stationary, steady wind is well known (Section S1.5.3 in S1 Text). Eq (7) reduces to the familiar Ekman pumping $w_{\mathrm{E}} = \mathrm{curl}\, \tau/(\rho_{\mathrm{o}} f)$. Since below the mixed layer, geostrophy gives $w_z = -(u_x + v_y) = 0$, a vertically uniform column of vertical velocity equal to the Ekman pumping is expected [Section S1.5.3 in S1 Text; 21, see *his* Fig. 4.13.3]. To reconcile with the bottom boundary condition that $w|_{z=-D} = 0$, a bottom boundary is necessary; otherwise, this state cannot exist.

3.7.2 Equilibrium response. If we relax the requirement that $\partial_t = 0$ for all variables and assume only that $\partial_t w$ is *constant in time*, (7) reduces to the familiar Ekman pumping $w_{\mathrm{E}} = \mathrm{curl}\, \tau/(\rho_{\mathrm{o}} f)$ again and we obtain an equilibrium solution Eq. (S42) in S1 Text, which satisfies $w|_{z=-D} = 0$. To reproduce it here,

$$w = \frac{(z+D)g}{f^2} \nabla^2 \eta_t \tag{8a}$$

$$= \frac{z+D}{D} w_{\mathrm{E}}. \tag{8b}$$

That is, w has a linear profile up to the bottom of the Ekman layer.

The problem with this solution is that the sea level keeps dropping because of the Ekman divergence. As seen below, the response to a moving TC is analogous to this state except that the sea level does not keep dropping there because the TC is moving.

3.7.3 Moving TC. Here we discuss only the results; the derivation is detailed in Section S1.5.4 in S1 Text. When the TC is moving at a steady speed of C_{tc}, the vertical profile of w is still linear as in (8b), and (7) can be written as

$$(C_{tc}^2\partial_x^2 + f^2)w_E = f\,\mathrm{curl}\,\tau/\rho_o \tag{9}$$

in the moving coordinates. The solution can be written as a zonal convolution integral between curl τ and the Green's function (S45) in S1 Text. This integral is again easily evaluated numerically on a grid as discussed (Eq. S1.3.4) in S1 Text for the solution shown in Fig 9. This solution agrees fairly well (Fig 17) with the actual w at z = 200–300 m, where w takes its peak value (Fig 13G).

In the uniform-density solution, the oscillation continues at a constant amplitude and its wavelength is $C_{tc}/|f|$ (Eq. S45) in S1 Text, which is the wavelength in the limit that $c_n^2 \ll C_{tc}^2$, a good approximation for a typical TC translation speed (see Eq 5). Indeed, in that limit, the "w-equation" (1) for each mode n reduces to

$$(C_{tc}^2\partial_x^2 + f^2)(-w_n) = a_n' f\,\mathrm{curl}\,\tau/\rho_o,$$

which indicates that $-w_n/a_n' = w_E$ for all $n \geq 1$. As we mentioned earlier, our sign convention means that $-w_n$ is proportional to the mode's contribution to the 3-d w and the factor a_n' is the nondimensional weight for each mode. In this limit, the peaks of all baroclinic modes coincide with that of the delayed Ekman pumping (9) and the resultant perfect vertical alignment would lead to the columnar w.

These observations suggest that the uniform-density solution can be viewed as a limit that $c_n \to 0$ for all baroclinic modes ($n \geq 1$). That interpretation is supported by the result shown in Section S1.2.5 in S1 Text that in the limit of weak stratification, the baroclinic c's all approach zero with the eigenfunctions changing little, whereas the barotropic mode changes little.

In the actual solution, the amplitude slowly decays to the west because the vertical modes gradually lose vertical alignment (Section 3.4.1). In the meridional profile (Fig 14B), the double-peak structure, reflective of the structure of the wind curl (Fig 11), is more pronounced in the delayed Ekman pumping than in the actual w. This must be because with a finite c_n, the impacts of curl are spread meridionally by inertio-gravity waves, whereas for the uniform-density ocean, solution takes the form of a pure zonal integration of wind curl (Eq. S45) in S1 Text.

As expected, the sea level response of this uniform-density solution is almost identical to that of the barotropic mode (Section S1.5.4 in S1 Text).

4 Summary and discussion

4.1 Summary

To explore the impacts of a tropical cyclone (TC) on the oceanic circulation near the sea floor in a deep sea, we construct a 4-d solution to a set of linearized primitive equations (S1) in S1 Text on an f plane with a flat bottom at $z = -D$ and constant density stratification N forced by wind stress and atmospheric pressure anomaly from an axisymmetric empirical model TC (Section S1.4 in S1 Text) that moves at a constant speed C_{tc}. To do so, we expand each dependent variable into vertical modes, numerically solve the reduced-gravity model (RGM) of each

mode, and superpose the solutions to obtain the 4-d field (Section S1.2 in S1 Text). To verify and interpret the numerical solutions of the RGM, we use the Green's functions, semi-analytic solutions, and numerical solutions to the "w-equation" (Eq 1; see Section S1.3 in S1 Text).

4.1.1 Barotropic response. The barotropic mode responds to the TC's low pressure (p_a) with an almost matching sea level rise, canceling the low pressure and generating little horizontal flow (Fig 3). This "isostatic" balance holds because $C_{tc}^2 \ll c_0^2$ and $L^2 \ll \alpha_0^{-2}$, where $c_0 = \sqrt{gD}$ is the barotropic gravity-wave speed, L is the horizontal characteristic scale of p_a, and $\alpha^{-1} \equiv c_0/f$ is the barotropic Rossby radius. Both conditions are usually satisfied for TCs. The only significant response is the upwelling that feeds the sea-level rise in front of the TC and the matching downwelling that restores the sea level behind the TC (Fig 4). It is $\mathcal{O}(1 \times 10^{-5}\mathrm{m/s})$ (Fig 4) and linearly decreases to zero at the bottom. This is not insignificant but it is an order of magnitude smaller than the baroclinic w to be discussed below.

The barotropic response to the TC's wind stress is a permanent sea level drop due to the (barotropic component of) Ekman divergence behind the TC (Fig 7). The resultant pressure anomaly is roughly $\sim$2 hPa. The vertical velocity associated with this motion is a very small downwelling which is $\mathcal{O}(1 \times 10^{-7}\mathrm{m/s})$ at the surface and linearly decreases to zero at the bottom (Fig 5). The horizontal scale of the pressure drop, $\sim$400 km, is significantly limited by the negative curl surrounding the positive curl of the TC core (Fig 6). This is because even though the amplitude of the negative curl is weak, its area is much broader than that of the positive core.

4.1.2 Baroclinic response. The baroclinic response to p_a is negligible because this forcing term enters the primitive equation as a vertically-uniform body force (Eq. S3) in S1 Text, whose contribution to each mode is proportional to the vertical integration of the p-mode functions, $\psi_n(z)$, and the vertical integration is negligibly small for all baroclinic modes.

The baroclinic response to winds takes a form of the well-known train of waves (Figs 8 and 11). Its streamwise wavelength is approximately $2\pi\sqrt{C_{tc}^2 - c_n^2}/f$, and the angular frequency is $C_{tc}f/\sqrt{C_{tc}^2 - c_n^2}$. As the mode number n is increased, the zonal wavelength gradually increases and approaches the constant value $2\pi C_{tc}/f$, and the frequency gradually decreases and approaches the constant value f. Both are, however, already close to the final value because $C_{tc}^2 \gg c_n^2$.

The first peak of upwelling comes about a quarter wavelength behind the center of the TC (Figs 8 and 11) and a regular oscillation in w follows. The net impact of the wave train is a permanent pressure drop in the upper ocean, lowered sea level, and cooling near the surface (Figs 10 and 11).

The lateral scale of the first upwelling peak is almost that of the TC's core of positive curl τ (Figs 8C and 9C) because the lateral scale of the meridional propagation (Eq 6) is smaller than that of the TC's core at this point. The subsequent peaks in the wake gradually spread as a packet of inertio-gravity waves; this spread is naturally larger in lower modes (Fig 9A) and smaller in higher modes (Fig 12A).

4.1.3 4-d structure. The most striking feature of the superposed w field (Fig 13) is the column of upwelling that linearly grows from zero at the bottom to its maximum near the bottom of the mixed layer (Fig 13G). This structure is a result of the vertical coherence of the modes: all baroclinic modes have the first peak in w_n approximately here. This vertical coherence is gradually lost because the zonal wavelength lengthens for higher modes. The lateral spread of the wave train also reflects the speed difference between modes (Eq 6; Figs 8 and 11).

Viewed as a collection of near-inertial waves, this pattern may be interpreted as a "lee wave" response, except that the wind curl of TC initially generates the disturbance throughout the water column, not just within the mixed layer. For this reason, the near-inertial waves appear

near the bottom quickly without waiting for the wave packets to propagate downward at the very slow vertical group velocity.

As expected, upwelling wins on average and the wave train leaves a region of colder water. The density anomaly increases from zero at the bottom to its maximum value at the bottom of the mixed layer (Fig 15). The lateral convergence of water that feeds the upwelling creates this density structure.

The pressure anomaly is dominated by the barotropic response to wind curl. The pressure drop starts $\sim$400 km before the TC center and completes $\sim$400 km after the center (Fig 16). The lateral spread is of a comparable scale (Fig 16) because the w response is approximately circular (Fig 5).

The baroclinic modes modifies this pressure field with their near-inertial oscillation. Since this oscillation starts with negative and positive pressure anomalies in the upper and lower oceans (Fig 16E), it reinforces and weakens the barotropic pressure anomaly in the upper and lower oceans, respectively (Fig 17). The first negative peak in pressure anomaly at the bottom is delayed (Figs 16A and 17B) as a result.

4.1.4 Uniform-density ocean. The same moving wind stress curl drives a train of inertial oscillation in the linearized primitive equations without stratification ($N = 0$). The streamwise structure of this w field is a simple inertial oscillation very similar to that of the numerical solution (Fig 14A) and its vertical structure is the same as that of the first upwelling column of the numerical solution (Fig 13), that is, a linear profile from the bottom to the bottom of the mixed layer. This solution is a response to the "delayed Ekman pumping" (7) and can be regarded as a limit that $c_n \to 0$ for $n \geq 1$ and thus explains the solution with a stratification because $c_n^2 \ll C_{\mathrm{tc}}^2$ for $n \geq 1$.

4.2 Discussion

4.2.1 Typhoon composites. The composite vertical profile of w from the OGCM in Fig 2 has some similarity and some discrepancies with that of our idealized theoretical calculation in Fig 13G. The theoretical amplitude, which is the same as that of the delayed Ekman pumping according to our interpretation (Section 3.7), is 4×10^{-4} m/s and that of the composite (Fig 2) is about 1×10^{-3} m/s or somewhat larger.

The central pressure of this TC is about 985 hPa at the time of Fig 2A and it was about 960 hPa one day before when the TC center was at about 26˚N. The ambient pressure, though hard to estimate visually, seems to be about 1015 hPa in Fig 2A. That is, $\Delta P \sim$ 30–55 hPa, which is 1.5–2.5 times the value we have used for the theoretical calculations. Near the center of the TC, where the centrifugal force dominates [e.g., 22, and references therein], the squared wind speed, and hence the wind stress, is proportional to ΔP (Section S1.4 in S1 Text) and therefore the magnitude of w is roughly proportional to ΔP. The theoretical amplitude is, hence, not inconsistent although more detailed comparison would be necessary to give a more reliable answer.

The peak depth is $\sim$1000 m for the composite (Fig 2B). The mixed layer cannot be this deep and, if our interpretation of the depth profile is correct, this discrepancy must be because of noise, including tides and other flows, which are not directly driven by the TC.

At this point, however, we do not attempt further detailed comparisons because we do not know how representative the composite Fig 2 is. We just show the one that looked the most clean among the several composites we looked at. Although strong vertical velocity reaching near the bottom was a common feature, the vertical profiles varied (not shown).

JCOPE-T includes tidal forcing generating barotropic tides, and large-scale internal tides are also abundant in the model [23, 24]. This may be one of the reasons why the composites differ so much between different typhoons (not shown).

To find common features, we trialed composites of low-pass-filtered data. Specifically, we applied a Hann filter with a half window size of 24 hours at each spatial point before calculating the temporal anomaly. That is,

$$\text{anomaly}(t) = \text{low-pass-filtered}(t) - \text{temporal mean},$$

where the period of the temporal average is ±4 d around the TC's time. The composite now showed a much smoother and more systematic vertical velocity field (not shown). Since the timescale of smoothing much reduces the near-inertial oscillation, the vertical profile of this smoothed field is no longer that of the first upwelling peak. Also, the direction of the zonal and meridional sections are different from the angle of the TC track and therefore the temporal average includes variability somewhat outside the variability directly behind the TC.

Also, many typhoons rapidly change their courses or their speeds or both during their traversal south of Japan. (One can confirm this by looking at the "best track" dataset described in Section S1.1.1. in S1 Text) Composites like Fig 2 may not capture the core of the upwelling column.

The best approach would therefore be 1) use another high-resolution model that does not include tides, 2) choose TCs that traveled in a relatively straight line, 3) discard the portion of the track where the TC's speed changed drastically, and 4) set the vertical section along the track, not in the meridional or zonal direction. This would be an interesting future project.

4.2.2 TC speed. Our analysis has been benefited from the parameter range that $c_n^2 \ll C_{\text{tc}}^2 \ll c_0^2$ for all $n \geq 1$. (Even though $c_1 \ll C_{\text{tc}}$ does not hold, $c_1^2 \ll C_{\text{tc}}^2$ does.) When C_{tc} is faster, not much changes (as long as $C_{\text{tc}}^2 \ll c_0^2$). The dependency of the frequency and wavelength of the near-inertial oscillation on c_n will be even weaker (see Eq (5) and discussion below it) and the frequency will become even closer to f. Consequently the dispersion of the near-inertial waves behind the TC (Fig 13) will be weaker still. The triangle of causality (Eq (6), the wedge shape behind the TC in Fig 8) will become narrower. When C_{tc} is slower, the frequency and wavelength will become somewhat more sensitive to c_n (Eq (5)) and the inertial oscillation will be somewhat more dispersive. The triangle of causality will become wider.

An interesting question is what happens when $C_{\text{tc}} \approx c_1$, although such a situation is rare [6]. Trying to see what happens, we ran our RGM with $C_{\text{tc}} = c_1$. The response was weak and noise was relatively large (not shown). This is understandable. As $C_{\text{tc}} \to c$, the Green's function for $C_{\text{tc}} > c$ (Eq. S25 in S1 Text) becomes wigglier (its wavenumber becoming shorter and shorter) in the x direction and that for $C_{\text{tc}} < c$ (Eq 3) becomes narrower. Finite-difference error would inevitably contribute. To solve this problem for a finite-difference model, one would need to introduce some form of spatial mixing.

On the other hand, this is not a resonance. When $C_{\text{tc}} = c_n$, the left-hand-side operator of the w-equation (1) becomes $\partial_y^2 - \alpha_n^2$ and allows for a finite solution with a simple Green's function (not shown). Because there is no x dependency, the solution would retain the x structure of the forcing and integration happens only in the y direction.

One approach would therefore be to replace the numerical RGM with convolution integrals like (S28) in S1 Text for all baroclinic modes. To obtain other fields than w, one would use the convolution integrals of [12]. Even though the numerical RGM is much more versatile, being applicable to a much wider variety of situations (what if the TC's track isn't straight, for example?), this kind of semi-analytic approach would cover a wider range of C_{tc} for the simplest situation we have been looking at.

4.2.3 Limitations and potential extensions. Obviously, our linear model lacks horizontal advection of momentum and density and therefore nonlinear impacts such as enhanced mixing [25] are missing. The potential trapping of small-scale near-inertial waves by relative vorticity [20, 26, e.g.] is also missing. Jaimes & Shay [27] reported *upward* energy propagation of near-inertial waves with wavelengths of $\sim$ 200 –300 m in their observation, whereas our results include only a large-wavelength near-inertial waves whose energy propagates downward. This feature could also be due to some subsurface nonlinear processes.

The large-scale (lower-mode) part of the inertial oscillation (Fig 13) would probably be affected less by advection because of its higher group speeds, but how nonlinearity affects the near-bottom anomaly field would be an interesting subject of future studies.

Another process missing from our model is the deepening of the mixed layer due to the increased turbulent mixing [e.g., 3, and references therein]. Assessing this impact on the basis of the present study's results, we conjecture that the deepening can be simply handled by changing h_{m}. Since this is a vertical mixing, the overall weight of the water column is not affected and the impacts on the bottom pressure would be small.

We used a constant stratification for simplicity and in hindsight this was a good choice because a more realistic stratification would not bring about something significantly new. The relation between n and c_n^{-1} is no longer linear with a more realistic stratification, but the property that c_n decreases as n increases stays. Because of the different n–c_n relation, the phase lines behind the TC in Fig 13A would take somewhat different curvatures and vertical profiles of w in the wake further down (after the dispersion of the vertical modes) would be different. For example, The vertical profile of w away from the TC track in Fig 13B is similar to $\sin \pi z/D$ because that is the vertical profile of $\Psi_1(z)$ for mode 1 with N = const. With a more realistic $N(z)$ with a typical pycnocline, the vertical profile of mode 1 has its peak near the pycnocline [15]. Crucially, however, the vertical column of w just behind the TC would not change depending on N (Section 3.7).

Presence of lateral boundaries would not affect the equilibrium response to TC since the main oceanic response is the columns of near-inertial oscillation, which do not propagate far, behind the TC.

If the planetary beta is included, the anomalies behind the TC would slowly propagate as Rossby waves. In addition, if the TC moves in the meridional direction, the frequency of the near-inertial oscillation behind the TC should depend on latitude. It would be interesting to explore how these elements modify the solution we have obtained.

Finally, the flat bottom assumption was necessary for the modal-decomposition approach to work. The column of strong vertical velocity may induce strong currents on bottom slopes, which in turn may affect bottom pressure anomaly.

4.2.4 Bottom pressure. In the introduction, we mentioned an observation in which the bottom pressure starts to decrease as a TC's center approaches and reaches its minimum ($\Delta p \sim 2$ hPa) 1–2 d later. Although our result shown in Fig 16 is not inconsistent with the observation, there is still too much uncertainty to draw any conclusion from this comparison.

We looked at the vertical velocity anomalies in JCOPE-T and recognized strong w anomaly extending upward from the Bonin Trench slope (not shown) next to the observational site. This feature may be an indication of enhanced local circulation, which may or may not be due to the TC and may or may not be affecting the bottom pressure anomaly.

The motivation of this comparison is two-fold: one is to validate and extend our simple linear model and the other is to provide the observationalists with information as to what signal one would expect from TCs. For both purposes, we would need to look at more observational data and to analyze OGCMs in more details.

Supporting information

S1 Text. Appendices. Details of the methods are provided. Auxiliary datasets and methods of their analyses are described.
(PDF)

S1 Dataset. Sea-floor pressure measurement. A netCDF data file containing the hourly-averaged sea-floor pressure in Pa at the "B06" station of [1] from 2015-08-05T00:00:00Z to 2015-08-16T00:00:00Z. An arbitrary uniform offset has been subtracted from the pressure values.
(NC)

S2 Dataset. JCOPE-T station subset. NetCDF files containing the hourly-mean potential temperature (`B06-tm-2015.08.05-2015.08.16.nc`), salinity (`B06-sm-2015.08.05-2015.08.16.nc`), and sea level (`B06-em-2015.08.05-2015.08.16.nc`) from 2015-08-05T00:00:00Z to 2015-08-16T00:00:00Z from the JCOPE-T-NEDO model [23, 29] at the closest gridpoint to the "B06" station of [1]. The hourly atmospheric pressure data that forced the model [23] is also included (`B06-slpmhour-2015.08.05-2015.08.16.nc`); this data is interpolated to the same mid-hour time as the hourly-mean model data is defined at.
(ZIP)

S3 Dataset. JCOPE-T sea-level pressure subset. NetCDF file containing two snapshots, at 2014-11-06T06:00:00Z and 2015-08-10T18:00:00Z, of the sea-level pressure data that forced the JCOPE-T model.
(GZ)

Acknowledgments

We would like to thank Kosuke Ito for discussion about typhoons. Thanks are extended to Toshiyuki Hibiya, Jay McCreary, Kensuke Nakajima, Hideharu Sasaki, Yuki Tanaka, and Akira Yamazaki (alphabetical order) for helpful discussion. Comments from anonymous reviewers and the handling editor helped improve the manuscript. The OGCM used here is called JCOPE-T, part of the JCOPE project at JAMSTEC (https://www.jamstec.go.jp/jcope/). The JCOPE-T data we use in the present study is available either as Supporting Information "S2 Dataset" and "S3 Dataset" or from the zenodo repository (https://doi.org/10.5281/zenodo.13132471). See Section S1.1.2 in S1 Text for details. The bottom-pressure observation [1] was supported by JSPS KAKENHI Grant Number JP25247074. The pressure-gauge data used for Fig 1B is provided as Supporting Information "S1 Dataset". To plot most of the figures, we have used the graphics package "Makie" [28], https://docs.makie.org/] of the Julia language. Special thanks go to Julius Krumbiegel, who answered many novice questions from RF about Makie. We also used the PyFerret program to plot some of the figures. PyFerret is a product of NOAA's Pacific Marine Environmental Laboratory. (Information is available at http://ferret.pmel.noaa.gov/Ferret/).

Author Contributions

Conceptualization: Ryo Furue, Yoshio Fukao.

Data curation: Hiroko Sugioka.

Formal analysis: Hiroko Sugioka.

Investigation: Ryo Furue, Yoshio Fukao.

Writing – original draft: Ryo Furue.

References

1. Fukao Y, Kubota T, Sugioka H, Ito A, Tonegawa T, Shiobara H, et al. Detection of "rapid" aseismic slip at the Izu-Bonin Trench. J Geophys Res Solid Earth. 2021; 126(9):e2021JB022132. https://doi.org/10.1029/2021JB022132
2. Blackman RB, Tukey JW. The Measurement of Power Spectra: From the Point of View of Communications Engineering. Dover Publications; 1959.
3. Zhang H, He H, Zhang WZ, Tian D. Upper ocean response to tropical cyclones: a review. Geosci Lett. 2021; 8(1):1. https://doi.org/10.1186/s40562-020-00170-8
4. D'Asaro EA, Black PG, Centurioni LR, Chang YT, Chen SS, Foster RC, et al. Impact of Typhoons on the Ocean in the Pacific. Bull Am Meteorol Soc. 2014; 95(9):1405–1418. https://doi.org/10.1175/BAMS-D-12-00104.1
5. Ezer T. Numerical modeling of the impact of hurricanes on ocean dynamics: sensitivity of the Gulf Stream response to storm's track. Ocean Dynamics. 2019; 69(9):1053–1066. https://doi.org/10.1007/s10236-019-01289-9
6. Fujii T, Mitsuta Y. Simulation of winds in typhoons by a stochastic model. Journal of Wind Engineering. 1986; 1986(28):1–12. https://doi.org/10.5359/jawe.1986.28_1
7. Geisler JE. Linear theory of the response of a two layer ocean to a moving hurricane. Geophys Fluid Dyn. 1970; 1(1-2):249–272. https://doi.org/10.1080/03091927009365774
8. Yang CY, Yang YJ, Tseng YH, Jan S, Chang MH, Wei CL, et al. Observational evidence of overlooked downwelling induced by tropical cyclones in the open ocean. Sci Rep. 2024; 14:335. https://doi.org/10.1038/s41598-023-51016-0 PMID: 38172221
9. Kuwano-Yoshida A, Sasaki H, Sasai Y. Impact of explosive cyclones on the deep ocean in the North Pacific using an eddy-resolving ocean general circulation model. Geophys Res Lett. 2017; 44(1):320–329. https://doi.org/10.1002/2016GL071367
10. Pedrosa-Pàmies R, Conte MH, Weber JC, Johnson R. Hurricanes Enhance Labile Carbon Export to the Deep Ocean. Geophys Res Lett. 2019; 46(17-18):10484–10494. https://doi.org/10.1029/2019GL083719
11. Spencer LJ, DiMarco SF, Wang Z, Kuehl JJ, Brooks DA. Asymmetric oceanic response to a hurricane: Deep water observations during Hurricane Isaac. J Geophys Res Oceans. 2016; 121(10):7619–7649. https://doi.org/10.1002/2015JC011560
12. Shay LK, Elsberry RL, Black PG. Vertical Structure of the Ocean Current Response to a Hurricane. J Phys Oceanogr. 1989; 19(5):649–669. https://doi.org/10.1175/1520-0485(1989)019%3C0649:VSOTOC%3E2.0.CO;2
13. McCreary JP. A linear stratified ocean model of the equatorial undercurrent. Phil Trans Roy Soc Lond A. 1981; 298:603–635. https://doi.org/10.1098/rsta.1981.0002
14. Chelton DB, de Szoeke RA, Schlax MG, El Naggar K, Siwertz N. Geographical variability of the first baroclinic Rossby radius of deformation. J Phys Oceanogr. 1998; 28(3):433–460. https://doi.org/10.1175/1520-0485(1998)028%3C0433:GVOTFB%3E2.0.CO;2
15. Gill AE. Atmosphere-Ocean Dynamics. San Diego: Academic Press; 1982. Available from: https://archive.org/details/atmosphereoceand0000gill/.
16. Kelly SM. The vertical mode decomposition of surface and internal tides in the presence of a free surface and arbitrary topography. J Phys Oceanogr. 2016; 46(12):3777–3788. https://doi.org/10.1175/JPO-D-16-0131.1
17. McCreary JP, Shetye SR. Observations and Dynamics of Circulations in the North Indian Ocean. Atmosphere, Earth, Ocean & Space. Singapore: Springer Nature; 2023. Available from: https://link.springer.com/10.1007/978-981-19-5864-9.
18. Tanaka Y, Hibiya T, Sasaki H. Downward lee wave radiation from tropical instability waves in the central equatorial Pacific Ocean: A possible energy pathway to turbulent mixing. J Geophys Res Oceans. 2015; 120(11):7137–7149. https://doi.org/10.1002/2015JC011017
19. Morozov EG, Velarde MG. Inertial oscillations as deep ocean response to hurricanes. J Oceanogr. 2008; 64(4):495–509. https://doi.org/10.1007/s10872-008-0042-0
20. Oey LY, Inoue M, Lai R, Lin XH, Welsh SE, Rouse LJ Jr. Stalling of near-inertial waves in a cyclone. Geophys Res Lett. 2008; 35(12). https://doi.org/10.1029/2008GL034273
21. Pedlosky J. Geophysical Fluid Dynamics. 2nd ed. New York: Springer-Verlag; 1987.
22. Yan D, Zhang T. Research progress on tropical cyclone parametric wind field models and their application. Regional Studies in Marine Science. 2022; 51:102207. https://doi.org/10.1016/j.rsma.2022.102207

23. Varlamov SM, Guo X, Miyama T, Ichikawa K, Waseda T, Miyazawa Y. M2 baroclinic tide variability modulated by the ocean circulation south of Japan. J Geophys Res Oceans. 2015; 120(5):3681–3710. https://doi.org/10.1002/2015JC010739

24. Fukao Y, Miyama T, Tono Y, Sugioka H, Ito A, Shiobara H, et al. Detection of ocean internal tide source oscillations on the slope of Aogashima Island, Japan. J Geophys Res Oceans. 2019; 124(7):4918–4933. https://doi.org/10.1029/2019JC014997

25. Chang SW, Anthes RA. Numerical Simulations of the Ocean's Nonlinear, Baroclinic Response to Translating hurricanes. J Phys Oceanogr. 1978; 8(3):468–480. https://doi.org/10.1175/1520-0485(1978)008%3C0468:NSOTON%3E2.0.CO;2

26. Pallàs-Sanz E, Candela J, Sheinbaum J, Ochoa J, Jouanno J. Trapping of the near-inertial wave wakes of two consecutive hurricanes in the Loop Current. J Geophys Res Oceans. 2016; 121(10):7431–7454. https://doi.org/10.1002/2015JC011592

27. Jaimes B, Shay LK. Near-Inertial Wave Wake of Hurricanes Katrina and Rita over Mesoscale Oceanic Eddies. J Phys Oceanogr. 2010; 40(6):1320–1337. https://doi.org/10.1175/2010JPO4309.1

28. Danisch S, Krumbiegel J. Makie.jl: Flexible high-performance data visualization for Julia. Journal of Open Source Software. 2021; 6(65):3349. https://doi.org/10.21105/joss.03349

29. Wang S, Guo X, Morimoto A, Cao A, Tsutsumi E, Miyazawa Y, et al. Semidiurnal Internal Tides in a Shelf Sea South of Japan: Characteristics, Energetics, and Temporal variations. Progress in Oceanography. 2024; 222:103229. https://doi.org/10.1016/j.pocean.2024.103229